Evaporation of Sessile Microdrops studied with Microcantilevers

DISSERTATION

zur Erlangung des Grades "Doktor der Naturwissenschaften"

im Promotionsfach Physikalische Chemie

am Fachbereich Chemie, Pharmazie und Geowissenschaften

der Johannes Gutenberg-Universität Mainz

vorgelegt von

Master-Chem. Dmytro S. Golovko

geb. in Slavyansk (Ukraine)

Mainz, 2008

Dekan:

1. Berichterstatter:
2. Berichterstatter:

Tag der mündlichen Prüfung: April, 15, 2008

Die vorliegende Arbeit wurde unter Betreuung von Herrn Prof. Dr. Hans-Jürgen Butt im Zeitraum zwischen Oktober 2005 bis Dezember 2007 am Max-Planck-Institut für Polymerforschung, Mainz, Deutschland angefertigt.

Index

Introduction and Motivation

Evaporation of drops of liquids freely flying in air or sitting on a solid is a very common dynamic phenomenon which can be seen in everyday life. Evaporating drops tune many natural phenomena like clouds formation and rain fall, appearance of rainbow and fogs, thus being a crucial inseparable part of the gigantic atmospheric thermal and mass circulation. At the human scale, a number of technological and industrial processes depends severely on drop evaporation phenomena. Among them are heat transfer applications [1-4], the combustion of fuel, prevention degradation of coatings, ink-jet printing [5-7], surface modification [8-11] and various applications in microfluidics [12-15].

The rate of evaporation of free suspended drops depends mainly on the nature of the liquid and on some physical parameters of its surroundings, like temperature and pressure.

The rate of evaporation of sessile drops is additionally determined by the surface properties of solids, liquids and gases, and therefore its study can give a key to better understanding interfacial interactions. Moreover, processes occurring in a drop or on the solid surface can affect the evaporation rate and thus can be investigated.

It is already more that 100 years ago as Maxwell proposed the consideration of the evaporation rate as governed by the diffusion of molecules in the gas phase [16]. Since then, many refinements have been proposed to better describe the basic modes of evaporation of sessile drops depending on the wetting properties of the substrate [17-29]. These studies were mostly dealing with a quantitative description of either a change of the contact angle and contact area monitored by video systems [23, 27, 28, 30] or a change of mass monitored by a quartz crystal microbalance (QCM) [31, 32]. The smallest drop size analyzed was on the order of 10 μm or several nanograms.

An intriguing question is the dynamics of drop evaporation in its very last stages, when, for example, the Laplace pressure significantly increases, the vapor pressure according to the Kelvin equation increases, and surface effects play a predominant role. Neither the QCM nor video microscopy are suitable for tracking the evaporation to its very end, because the drops are too small. Recently, a nanomechanical resonator [33] was designed to monitor in time the mass variation of evaporating liquid droplets. The authors are capable of tracing the drop mass down to several femtoliters.

However, the question on the influence of surface effects on the last stages of the drop evaporation was not yet addressed.

By now, evaporation of sessile microdrops can be successfully accomplished on atomic force microscope (AFM) cantilevers [34, 35] due to their high sensitivity and possibility to partly trace the evaporation dynamics of small drops at high time resolution (below a millisecond). The drop causes the cantilever to bend, since the elastic response of thin solids is comparable with forces exerted by the drop over the three phase contact line and its contact area [36-39]. The Laplace pressure acting over the drop contact area and the surface tension pulling the drop at its rim are not enough to cause noticeable bending of a hard and thick solid (see schematics in Fig. 1A), while a hard and thin plate can be bent by typically a few hundreds of nanometers (see Fig. 1B). In general, when a drop is deposited on a cantilever several types of measurements can be performed: spring constant calibration of the cantilever (see Fig. 1C); sensing of drop evaporation by surface forces (see Fig. 1D); sensing drop evaporation by mass change; sensing of the heat exchanged during evaporation.

In this work, I present and discuss an extension to the technique based on the use of AFM cantilevers to trace the evaporation dynamics of drops by two means simultaneously. This allows, first, to monitor cantilever bending caused by surface tension and Laplace pressure inside the drop, second, to follow mass reduction due to the shift in resonance frequency during drop evaporation. The technique is assessed by tracing the evaporation dynamics of water drops from hydrophobic cantilevers. From both signals, cantilever bending and resonance frequency, drop parameters can be extracted. The technique is used to evaluate quantitatively the cantilever "overbending" arising at the last stages of the evaporation of water drops on hydrophilic cantilevers. In turn, I show how to calibrate AFM cantilevers loaded by drops [34] of different masses presenting an extension to the well-known added-mass method [40] for the spring constant calibration of AFM cantilevers [41].

The evaporation rate of microscopic drops is higher than that of macroscopic ones due to their highly curved surface. As a result, they have a higher vapor pressure at the liquid/gaseous interface than planar liquid surfaces or large drops. In this case nonequilibrium effects take place [42-45]. Thus the applicability of Young's equation for microdrops thus needed to be verified. Therefore I performed a series of experiments on evaporation of small drops in nearly saturated atmosphere. Conclusion on the significance of Young's equation for microdrops are drawn [46].

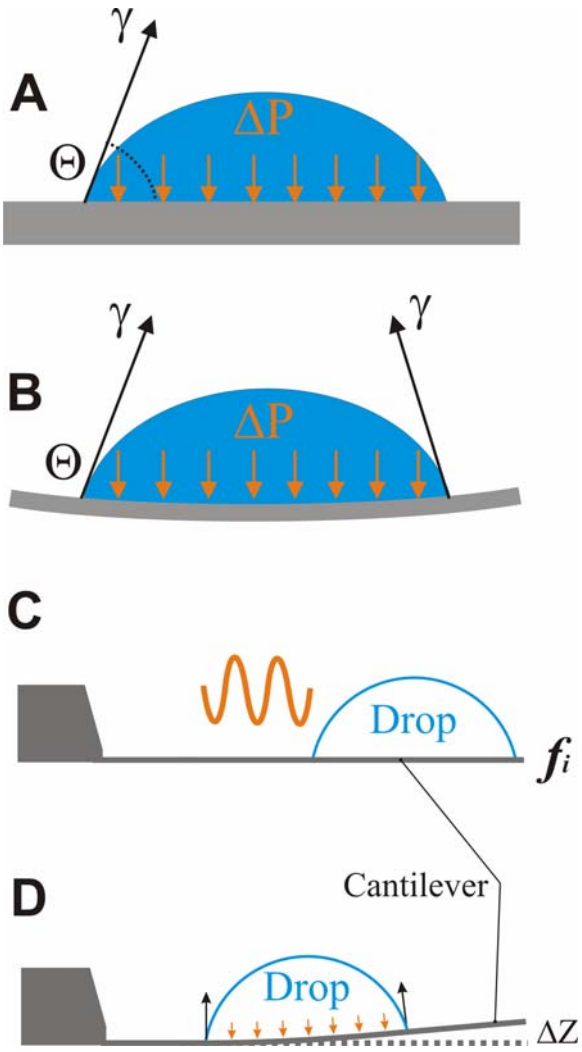

Figure 1. Drop on thick (A) and thin (B) solids. Two kinds of measurements on a cantilever: spring constant calibration (C), and evaporation tracing of small drops (D).

Chapter 1

Fundamentals

1.1 Young's Equation for Sessile Drops

When a drop of water or of another liquid is deposited on a flat underformable inert solid two cases are possible. First, the drop does not form a spherical cap and spreads until a thin liquid film is attained. Second, the drop establishes a finite contact angle. The first phenomenon is called complete wetting, when the contact angle $\Theta=0^o$. The second case is called wetting if $\Theta<90^o$, and non-wetting if $\Theta>90^o$. The contact angle Θ formed at the drop rim, also called three phase contact line (TPCL), is a result of the interplay of three interfacial energies, known as surface tensions, at the liquid/gas, γ, solid/liquid, γ_{SL}, and solid/gas, γ_S, interfaces (Fig. 2). The relationship between these components and the contact angle of the drop is described by Young's equation [47]:

$$\gamma \cos\Theta = \gamma_S - \gamma_{SL} \qquad (1)$$

This equation, strictly speaking, is valid when the contact angle is measured at equilibrium conditions, i.e. when the evaporation is negligible, the TPCL is not pinned, and we can neglect gravity. This is only possible for drops of typically a few millimetres in diameter, and ideally flat, chemically homogeneous surfaces. In the real world, however, a surface has always a certain degree of roughness, chemical heterogeneity or, simply, can be contaminated. The contact angle Θ_{eq} must be measured in equilibrium state. If the TPCL is moving (due to tilting of the substrate, excess/shortage of liquid, or evaporation), the measured contact angle can differ dramatically from Θ_{eq}. In this case, the value of the contact angle is an average of the measurements, and is called the dynamic contact angle. When the volume of a drop increases by constant adding of more liquid, the advancing contact angle, Θ_{adv}, is established. In the opposite case, by reducing the drop volume the receding contact angle, Θ_{rec}, is attained. Such a behavior, when $\Theta_{rec} < \Theta_{eq} < \Theta_{adv}$, is called

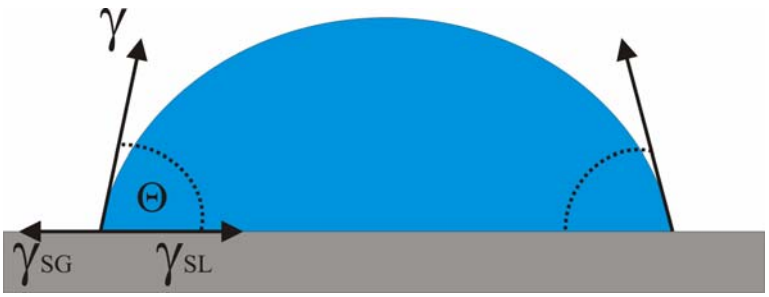

Figure 2. Sketch of a drop on a solid indicating three forces, the interfacial tensions, acting at the three phase contact line.

"contact angle hysteresis", and can give valuable information on solid surface properties, i.e. roughness, presence of contaminants, chemical heterogeneity, as well as surface active impurities dissolved in the liquid, metastable states of the wetting regimes, and in general it provides a quantitative parameter to describe deviations from the ideal surface.

On the validity of Young's equation for small drops.

The Young's equation, Eq. (1) can be used for a quantitative description of wetting phenomena, and yields good results with macroscopic drops. For them evaporation times are long enough (typically longer then 15 min), so that we can assume the drop in thermodynamic equilibrium, or quasi-thermodynamic equilibrium, while we measure the contact angle. The situation turns differently when we deal with a microscopic sessile drop. This drop is far from thermodynamic equilibrium due to the significant mass loss during the measurement time [42]. Moreover, even in saturated vapor atmosphere a drop evaporates due to the higher vapor pressure at the curved liquid surface, as stated by Kelvin's equation

$$P = P_0 e^{\frac{\lambda}{R_s}} \qquad (2)$$

where $\mathbf{R_s}$ is the radius of curvature of the drop, **P** is the vapor pressure of the liquid in the drop, and the parameter λ is a function of the temperature and the nature of the liquid and for many liquids is 1-3 nm. Thus the vapor pressure increases with decreasing drop size. As a result, the experimental conditions, while trying to measure an equilibrium contact angle for a microscopic drop, are almost never met in the earlier proposed derivations of Young's equation [36, 48, 49], since the mass exchange between the drop and its vapor atmosphere was ignored. Butt et al. in [46] introduced the

term “critical volume” of a drop, which allows us to discern whether Young’s equation can be used without limitations or it is of reduced significance. The critical volume $\mathbf{V_{cr}}$ is the volume of a drop evaporating in 15 minutes and depends on the properties of the liquid (saturation vapor pressure, molecular volume, and surface tension) and on the diffusion coefficient of its vapor in the background medium. If drops have volumina much larger than the critical volume, then mass decrease during evaporation can be ignored. Thus an equilibrium contact angle is measured, and we can apply Young’s equation. In the opposite case nonequilibrium effects become significant and Young’s equation can not be used appropriately.

1.2 Evaporation Dynamics of Sessile Drops

1.2.1 Modes of Evaporation

A drop can evaporate according to three main modes (Fig. 3), as revealed by the video-microscope images and well studied by now [19, 25, 50, 51]. When the contact angle, Θ, tends to remain constant during drop evaporation, the mode is called the Constant Contact Angle (CCA) evaporation. This mode is normally observed on smooth hydrophobic surfaces [52, 53], when the interactions between solid and liquid are expected to be small, and contact angles are normally about 90^o or higher. When a drop evaporates on a hydrophilic surface the preferential mode found to take place is the Constant Contact Radius (CCR) evaporation. That is, the radius of the drop, a, (Fig. 3) remains nearly constant over the whole evaporation process. Typical initial contact angles are lower then 40^o. The last mode is so-called Stick-Slip (SS) evaporation, when a decrease in the contact angle is followed by a decrease in the contact radius, and then, this process repeats itself several times. It is thus a combination of CCA and CCR modes of evaporation. This mode can be tuned by the surface nature, its roughness, its degree of contamination. In general, such surface properties may cause a pinning of the drop followed by the depinning, thus CCR and CCA mode can alternate with each other. Sometimes, the mixed mode is addressed when both the contact angle and contact radius change gradually with time. In turn the evaporation mode determines the evaporation rate.

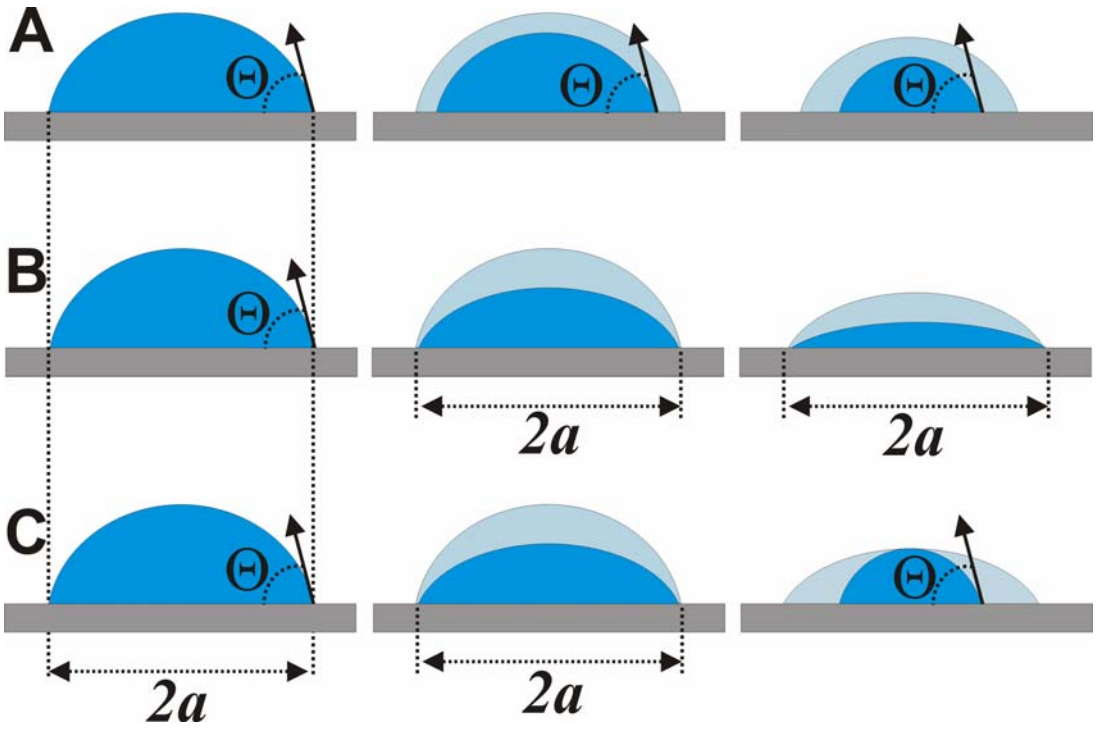

Figure 3. Modes of evaporation. A: with constant contact angle (CCA); B: with constant contact radius (CCR), and C: stick-slip mode (SS).

1.2.2 Evaporation Rate and Time for Sessile Microdrops

Let us again consider a drop deposited onto an underformable inert solid substrate. The shape of a drop of water is spherical if its diameter is smaller than 2.7 mm. This is stated by the equation

$$\kappa^{-1} = \sqrt{\frac{\gamma}{\rho g}} \qquad (3)$$

where $\boldsymbol{\kappa^{-1}}$ is the capillary length, ρ is the density of the liquid, and g is the acceleration of gravity. For water, γ_L=0.072 N/m, ρ=1g/cm^3 and **g**=9.8 m/s^2. Thus, $\boldsymbol{\kappa^{-1}}$ yields a criterion whether spherical [19] or ellipsoidal [54] geometry must be adopted to describe a sessile drop profile. Spherical geometry provides us with the advantage of the simplified treatment of the drop parameters evolution during the drop evaporation since the flattening effect due to gravity (hydrostatic pressure) can be neglected. In this case, a drop has a contact angle **Θ**, a drop cap radius ***a***, and a drop cap height ***h*** of the drop related with the drop radius $\boldsymbol{R_s}$, and the volume ***V*** of the drop (Fig. 4).

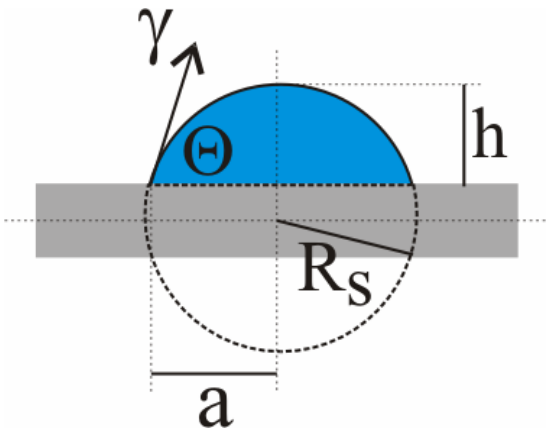

Figure 4. Geometry of a sessile drop on a solid inert underformable substrate.

$$R_s = a/\sin\Theta \quad (4)$$

$$h = R_s(1-\cos\Theta) \quad (5)$$

$$\Theta = 2\arctan(h/a) \quad (6)$$

$$V = \pi h(3a^2+h^2)/6 \quad (7)$$

In this work drops smaller than 100 μm were always used and the spherical geometry was applied to describe the drop profile. During evaporation the drop parameters change accordingly to the evaporation mode. It is normally observed that drops in CCR mode (on hydrophilic surfaces) evaporate faster than those evaporating according to CCA mode (on hydrophobic surfaces), since the drops are pinned. In general, surface properties, besides determining the evaporation mode, sensitively alter the evaporation rate [20, 27, 28, 55-58]. The evaporation rate analysis can be performed by applying a physical model developed earlier [19] to describe the evaporation drop volume in time, ***dV/dt***. For a drop in still air, evaporation is limited by the diffusion of molecules into air at the liquid/air interface. Assuming constant temperature and CCA evaporation the evaporation rate was calculated to be [19]

$$\frac{dV}{dt} = -2\pi D\frac{c_0 - c_\infty}{\rho} f\left(\frac{3V}{\pi\beta}\right)^{\frac{1}{3}} \quad (8)$$

Here, $\boldsymbol{D}$ is the diffusion coefficient of vapor molecules in the gas phase, $\boldsymbol{\rho}$ is the density of the liquid, $\boldsymbol{c_0}$ is the concentration of vapor molecules in direct vicinity to the liquid surface, and $\boldsymbol{c_\infty}$ is the concentration at infinite distance from the drop. $\boldsymbol{c_\infty}$ can be determined by the external vapor pressure

and the molecular mass M by $c_\infty = MP_v/k_BT$, where k_B and T are Boltzmann's constant and temperature. The concentration c_0 is given by the vapor pressure by Kelvin's equation (Eq. 2) rewritten as

$$c_0 = \frac{MP_0}{k_B T} e^{\frac{\lambda}{R_s}} \tag{9}$$

In equation (8) f and β are functions of the drop contact angle Θ and depend on temperature. The function β is expressed as

$$\beta = (1-\cos\Theta)^2(2+\cos\Theta) \tag{10}$$

For the function f several solutions were proposed[19, 28, 29]. Picknett & Bexon provided a polynomial[19]

$$f = 0.5\left(0.00008957 + 0.6333\Theta + 0.116\Theta^2 - 0.08878\Theta^3 + 0.01033\Theta^4\right) \tag{11}$$

where contact angle Θ can have values in the range of $10° \le \Theta < 180°$. Picknett & Bexon developed $f(\Theta)$ in power series by using the analogy between the diffusive flux and electrostatic potential. They converted the problem of determining the evaporation rate of a sessile drop to a problem of evaluating the capacitance of an isolated conducting body of the same size and shape as the drop as an equiconvex lens. It is related to the contact angle by applying Snow series.

The evaporation law for microscopic drops of pure liquids was derived by Butt et al [46]. The authors assumed CCA evaporation and neglected the cooling resulting from the vaporization. Two cases are considered. The first one deals with the evaporation of a water drop in its ***saturated vapor***, while the second one accounts also on ***non-saturation***. In saturated vapor the evaporation rate can be calculated by

$$\frac{dV}{dt} = -2\pi D \frac{P_0 V_m \lambda}{k_B T} f \tag{12}$$

where V_m is the molecular volume of the liquid phase, and P_0 is the external vapour pressure. After integration and rearrangement one obtains the evaporation time τ [46]

$$\tau = \frac{1}{2\pi} \cdot \frac{V_0}{D} \cdot \frac{k_B T}{P_0 V_m \lambda f} \tag{13}$$

here V_0 is the initial volume of the drop. The last term in Eq. (13) depends on the saturation vapour pressure, the molecular volume, the contact angle (in f), and on the surface tension of the liquid, since $\lambda = (2\gamma V_m)/(k_B T)$. The time constant τ depends linearly on the initial volume of the drop, meaning that the relative size V/V_0 of large drops decreases slower than the relative size of small drops. τ is the longest possible lifetime of a drop. And oppositely, if the evaporation lifetime is given the size of the drop can be calculated.

Practically, it is not possible to reach saturation for a prolonged time. To deposit a drop and to carry out a measurement the system needs a small opening. Also, differences in temperature in the measuring cell can cause gradients in vapor pressure. For microdrops the evaporation time can be calculated by [46]

$$\tau = \frac{1}{4}\left(\frac{3}{\pi}\right)^{\frac{2}{3}} \cdot \frac{V_0^{\frac{2}{3}}}{D} \cdot \frac{k_B T \beta^{\frac{1}{3}}}{P_0 V_m x f} \tag{14}$$

where $x=1-RH/100$ and RH is the relative humidity in %. To calculate the remaining volume V at each time step t we can use

$$V^{\frac{2}{3}} = V_0^{\frac{2}{3}} - \frac{4}{3}\pi D \frac{P_0 V_m}{k_B T} x f \cdot \left(\frac{3}{\pi\beta}\right)^{\frac{1}{3}} t \tag{15}$$

This equation contains no free parameters and states that the volume to the power of 2/3 decreases linearly with time. As an example, Figure 5 shows calculated times for evaporating drops in saturated (**A**) and non-saturated (**B**) vapor. For the latter case, the relative humidity was set to RH=99 %, that is $x=0.01$.

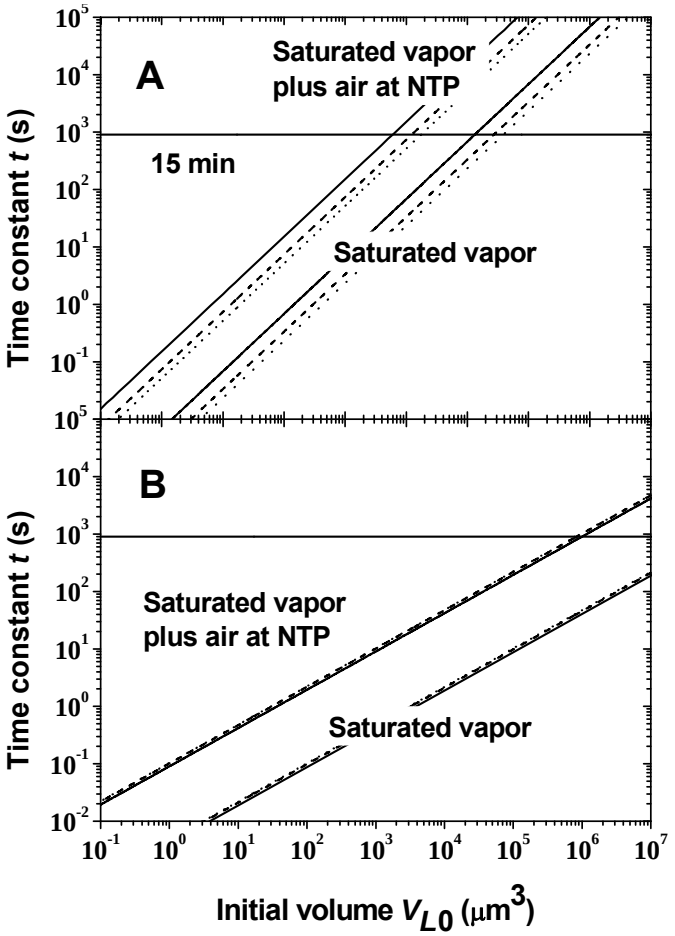

Figure 5. Time of evaporation of a sessile water drop at T=25°C versus the initial volume as calculated for RH=100% with Eq. (13) (A) and for RH=99% humidity with Eq. (14) (B). Time constants were calculated for evaporation in the presence of air at normal pressure (D = 2.4×10^{-5} m^2/s) plus saturated water vapor and without background gas, only in a saturated vapor atmosphere (D = 5.3×10^{-4} m^2/s). The contact angles were Θ = 30° (continuous line), 60° (dashed), and 90° (dotted). The initial volume of the drop varied from 0.1 μm^3 to 10^7 μm^3. The times scale ranges from 10 ms to ~1 day. The horizontal line indicates a typical observation time for a contact angle measurement of 15 min (from [46]**).**

For RH = 99% the evaporation time is much faster than for saturated vapor. That is, the evaporation rate depends strongly on the vapor pressure, which determines the diffusion coefficient of the vapor molecules. The higher the vapor pressure is, the smaller is the diffusion coefficient. Moreover, the evaporation time increases proportionally to $\tau \propto V_0^{\frac{2}{3}}$ rather than $\tau \propto V_0$, meaning that the evaporation for RH=99% depends rather on the diffusion coefficient than on the curvature of the liquid surface alone.

1.2.3 Surface Cooling due to Evaporation

When a drop spontaneously evaporates the most energetic molecules are leaving its surface. For this vaporization process the needed heat is provided by the ambient. As mentioned before, the evaporation mechanism is controlled by the diffusion of vapor into the ambient [18, 59, 60]. The role of the thermal properties of the substrate was not taken into account in any of these investigations. However, the thermal properties of the substrate may be limiting in the evaporation process [61]. The energy required for the evaporation is drawn from the environment by means of various mechanisms. If a drop is isolated then the drop cooling is determined by the evaporation rate.

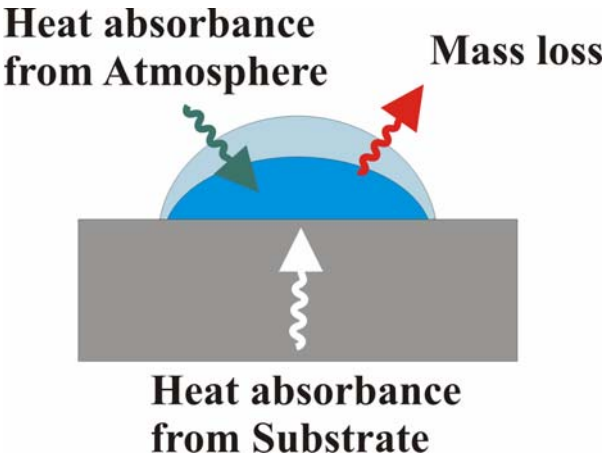

Figure 6. The scheme of the thermal and mass flows during the drop evaporation.

In the sessile drop case the cooling effect is also linked to the thermal properties of the substrate (Fig. 6). David et al. measured the temperature of the evaporating drop and demonstrated the role played by the substrate, i. e. its heat conductivity [62]. They measured temperatures at different positions inside a drop using a thermocouple. They found a difference between the temperature measured at the top of the drop and the ambient temperature of 1.75^{o}C for a 2 mm water drop on a PTFE (polytetrafluorethylene) surface, and 0.85^{o}C for a similar drop on an aluminium plate. The top of the drop was the coldest region compared with the ambient temperature. Such a difference in temperature within the drop induces small changes in the surface tension and generates Marangoni flows inside the drop. These effects were thoroughly investigated in a number of works [61, 63-65] and will not be discussed herein.

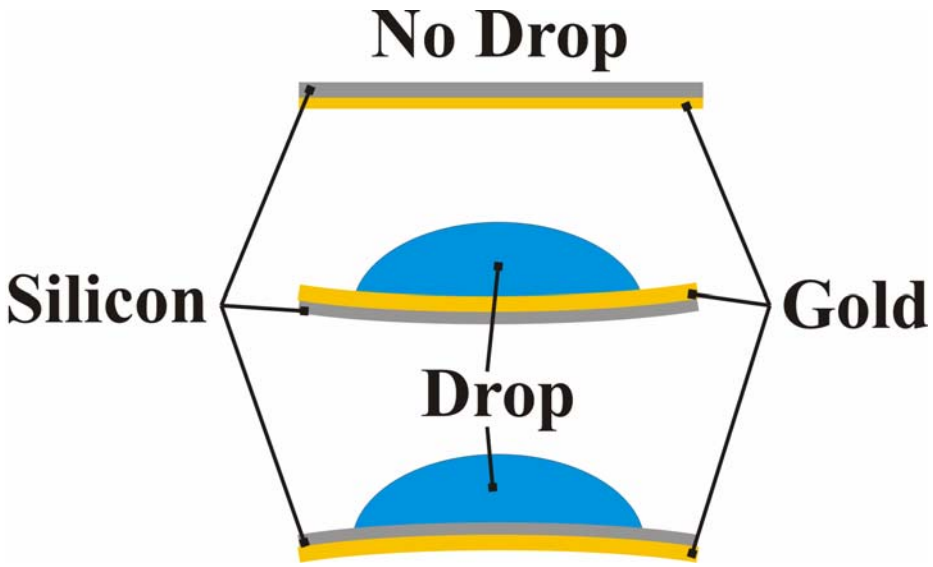

Figure 7. Schematics of the bimetallic effect on a gold coated solid with evaporating water drops on different sides.

A convenient way to measure surface cooling caused by the evaporation of drops can be implemented by utilizing the so-called "bimetallic" effect. That is when a sandwiched structure of two metal plates or a metal plate and another material (e. g. silicon, silicon nitride, etc.) deforms upon a temperature change due the different linear thermal expansion coefficients of the two materials. Schematically, this effect is illustrated in Figure 7. A water drop is placed either on the gold side of the gold/silicon sandwich or on the silicon side. Due to the higher thermal expansion of gold than silicon, and to the heat absorbed by the evaporating drop, the gold layer contracts causing an upward bending. The same drop deposited on the silicon side causes a downward bending. A direct method to measure surface cooling is to use cantilevers and the light lever technique utilized in atomic force microscopy. Thermally induced bending is typical for metal-coated cantilevers [66-68]. For uniform heating/cooling the bending $\boldsymbol{Z}$ of a cantilever is related to the absorbed heat and is expressed by

$$Z = \frac{5}{4}(\alpha_1 - \alpha_2)\frac{d_1 + d_2}{d_2^2 \phi}\frac{l^3}{(\lambda_1 d_1 + \lambda_2 d_2)w}W \qquad (16)$$

where $\boldsymbol{\phi}$ stands for a device parameter, $\boldsymbol{\alpha}$ are the expansion coefficients, $\boldsymbol{d}$ are the layer thicknesses, and $\boldsymbol{\lambda}$ the thermal conductivities, $\boldsymbol{l}$ and $\boldsymbol{w}$ the length and width of the bimetallic cantilever, and $\boldsymbol{W}$ the total power (heat absorbed by a drop in this case). A drop of water causes a local cooling underneath the contact area. It is not possible to calculate the resulting bending analytically: a numerical solution

of the problem is required. This can be done with the help of Finite Element Method simulations, described in more detail in the Experimental Chapter 2.

1.3 Sessile Drop on a Cantilever

It is instructive to mention the three time intervals into which a drop impact on a cantilever is divided [69-72](Fig. 8). In the beginning the drop hits the solid surface and spreads until it has reached its maximal contact radius and takes the shape of a spherical cap [69]. This spreading process is characterized by a time constant τ_s of about 1 ms for drops with a radius between 10 and 30 μm [72]. The impact of the drop causes the cantilever to oscillate. The initial oscillation is damped, and the amplitude decays exponentially with a time constant τ_d, which we measured to be between 2 and 10 ms in air. Finally, the drop evaporates from the cantilever and the time τ_e it takes is on the order of 1 s.

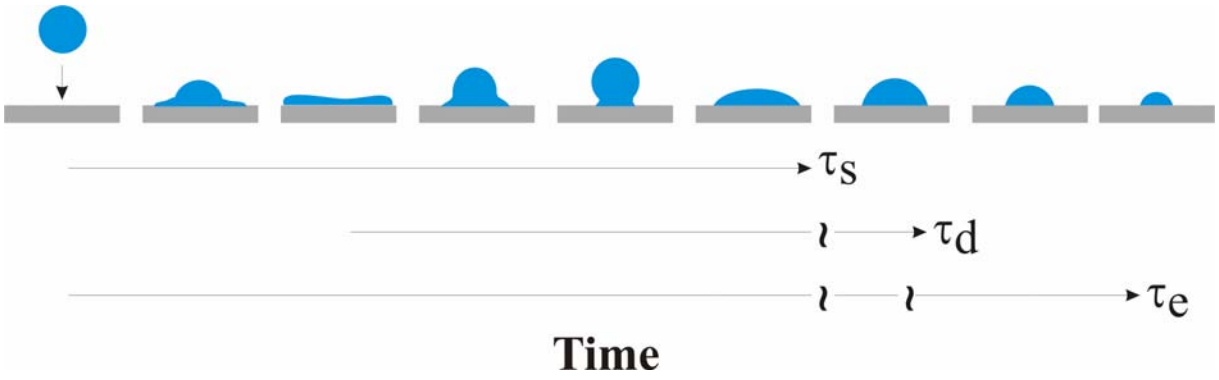

Figure 8. Sketch of the drop impact on a cantilever with related time constants (see the text for details).

1.3.1 Drop at the Free End of the Cantilever

At first, I consider the cantilever as a harmonic oscillator with a characteristic resonance frequency f_0 depending on its dimensions and mass. Second, I am interested in the second time domain τ_d, which is well separated from the other two, and is long enough to record the oscillations of the cantilever with a good time resolution. During τ_d the mass of the drop does not significantly change due to evaporation [46]. When a drop of mass m hits the cantilever with a velocity v_0 at t=0 I assume that its momentum is effectively transferred. The cantilever then oscillates at a frequency f_i correspondent to a deposited drop mass m_i (Fig. 9). Then the oscillations are dampened within τ_d. This process can be described by the equation of motion of the cantilever, assuming that no external forces are acting, and neglecting gravitation,

$$m^* \frac{d^2 z}{dt^2} + D\frac{dz}{dt} + Kz = 0 \qquad (17)$$

Here, z is the deflection of the cantilever, $\boldsymbol{D}$ is a damping coefficient, $\boldsymbol{m^*}$ is the effective mass, and $\boldsymbol{K}$ is the spring constant of the cantilever. Eq. (17) is valid for the deflection of the cantilever at its end and is independent of its form. For the special case of a rectangular cantilever, the spring constant is

$$K = \frac{Ewd^3}{4l_0^3} \qquad (18)$$

where $\boldsymbol{E}$ is Young's modulus of the material, $\boldsymbol{w}$ is the width, $\boldsymbol{d}$ the thickness, and $\boldsymbol{l_0}$ the length of the cantilever.

The effective mass is

$$m^* = m + aM \qquad (19)$$

where $\boldsymbol{m}$ the mass of the drop, $\boldsymbol{M}$ is the mass of the cantilever, and $\boldsymbol{a}$ is a form factor. For rectangular cantilevers $\boldsymbol{a}$=0.243 [73]. I ideally assume that the drop is

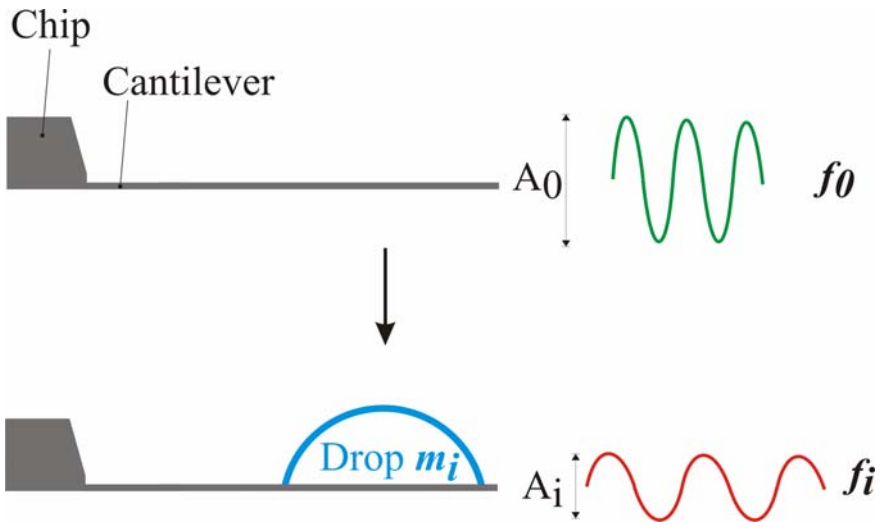

Figure 9. A drop deposited at the free end of the cantilever. f_i is a correspondent frequency of the cantilever loaded by a drop mass m_i (see Eq. (22))$_i$.

positioned at the free end of the cantilever and that the cantilever oscillates in its first oscillation mode [74, 75]. The general solution of Eq. (17) is

$$z(t) = -A_0 \sin(\omega t + \varphi) e^{-t/\tau_d} \tag{20}$$

with

$$\omega = 2\pi f = \sqrt{\frac{K}{m^*}} \tag{21}$$

and $\tau_d = 2m^*/D$. Initially, the deflection of the cantilever is zero, $z(t=0)=0$, which leads to $\varphi=0$. The negative sign in Eq. (20) takes into account that the falling drop causes the cantilever first to bend downward. Combining Eqs. (19) and (21), one can calculate the spring constant from the initial resonance frequency of the cantilever with the drop,

$$f_i = \frac{1}{2\pi}\sqrt{K/(m_i + aM)} \tag{22}$$

and the resonance frequency without the drop,

$$f_0 = \frac{1}{2\pi}\sqrt{\frac{K}{aM}} = \frac{1}{4\pi}\frac{d}{l_0^2}\sqrt{\frac{E}{a\rho}} \tag{23}$$

where ρ is the density of the material of the cantilever.
Rearranging Eq. (22) I obtain

$$m_i = K\frac{1}{(2\pi f_i)^2} - aM. \tag{24}$$

Equation (24) shows that if several drops of known masses are placed at the free end of a cantilever, and if the respective resonance frequencies are measured, a linear plot of drop masses versus $(2\pi f)^{-2}$ should give a straight line, the slope being the spring constant and the negative *Y*-axis intercept the

effective mass. This makes the method similar to the one proposed by Cleveland *et al* [40]. So far I discussed the ideal case of a mass placed at the very end of a cantilever. However, this can hardly be achieved in experimental practice. Figure 10A shows a rectangular silicon cantilever with a water drop on it, directly after impact. Like represented in the figure, the rim of the drop is at a certain distance from the free end of the cantilever. Nonetheless, also if we place the drop at the end (Fig. 10B), due to the spatial extension of the drop, its radius determines the distance of the center of mass. We must take this into account by considering the dependency of the spring constant on the position of the center of mass. For small distances this dependency can be approximated by

$$\frac{K}{l_d^3} = \frac{K_d}{l_0^3} \tag{25}$$

K_d is the measured spring constant for a drop of mass m_d, with its center of mass

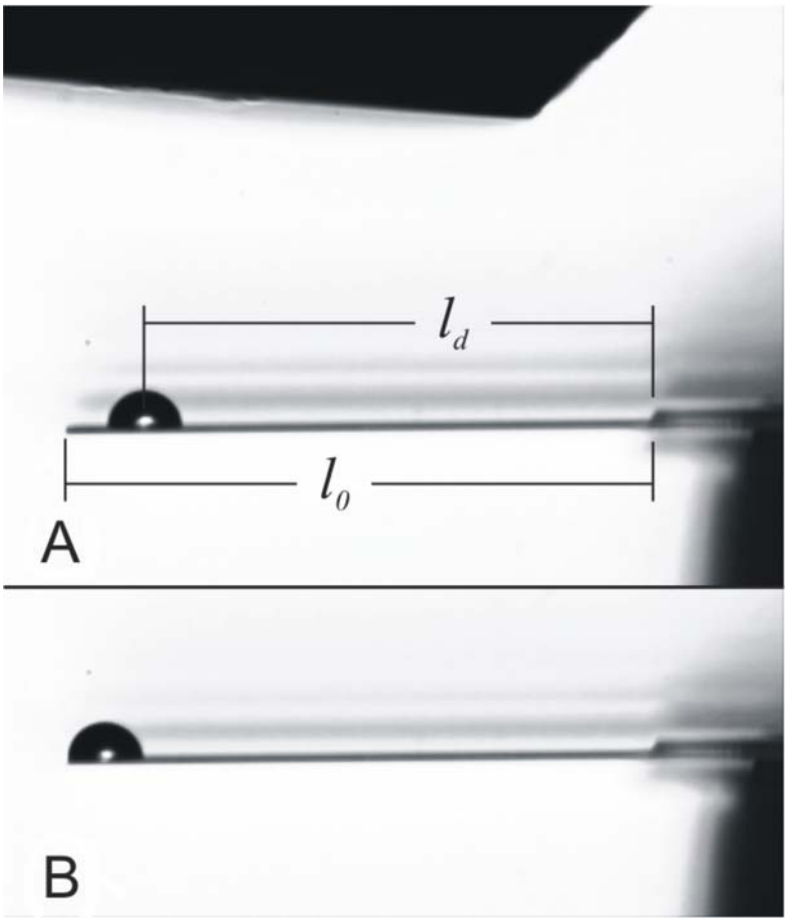

Figure 10. A microdrop of water close to (A) and at the end (B) of a rectangular silicon cantilever, directly after impact.

located at $\boldsymbol{l_d}$ from the base of a cantilever that has an overall length $\boldsymbol{l_0}$. *K* is then the spring constant if the same drop would have its center of mass located at the very end. I used Eq. (25) for calculating the spring constants of all examined cantilevers.

1.3.2 Drop in the Middle of the Cantilever

To describe the bending of a cantilever induced by the drop sitting on the top side for $t>>\tau_d$ a theoretical model must be developed. It was done by Bonaccurso and Butt in [34]. Here I briefly recap the results of their calculations. First, they assumed that the bending of the cantilever takes place at a slower time scale than the inverse resonance frequency, so that the cantilever is always in equilibrium with respect to a given drop shape. Second, several effects cause a bending of the cantilever:

- The normal component of the surface tension of the liquid and the Laplace pressure in the drop,
- The change in interfacial stress when the solid/vapor surface is replaced by a solid/liquid interface,
- The lateral component of the surface tension of the liquid,
- The line tension at the periphery of the drop, and
- The gravitational force due to the weight of the drop.

The effect of all contributions on the cantilever shape is further briefly discussed. First, the shape of the cantilever in a Cartesian coordinate system *XYZ* is calculated. This coordinate system originates in the center of the contact area of the drop (Fig. 11). The *X* axis is oriented along the cantilever parallel to the cantilever surfaces in the center of the drop. As the most relevant property, the inclination at the rim of the drop is derived. The resulting change in cantilever shape is supposed to be very small compared to the size of the drop. In a second step, Bonaccurso and Butt consider the shape of the whole cantilever, transforming the results to the coordinate system *xyz*, which originates at the base of the cantilever with a horizontal *x* axis. This is so-called 2.5D model since it comprises a 3D geometry for the application of the forces on the cantilever coupled to a 2D bending of the cantilever as considered above. Also in this model the cantilever is non-constrained, and thus an idealization [35].

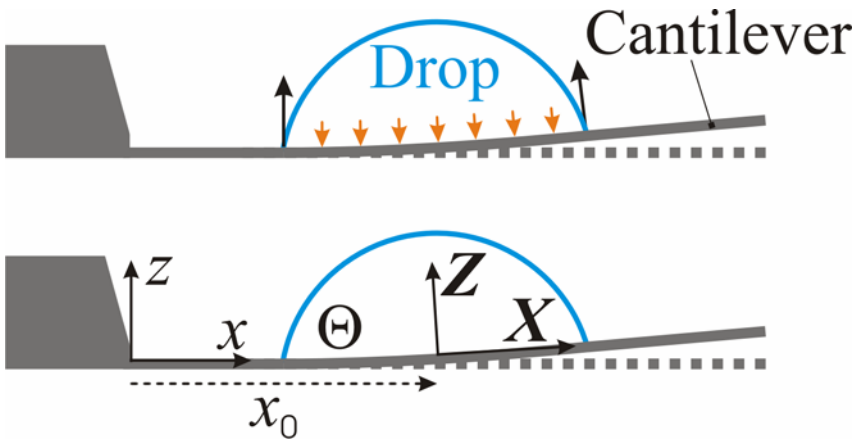

Figure 11. Side view of a drop placed on a cantilever which is fixed on the left side. The drop exerts a Laplace pressure over the whole contact area and a force due to the surface tension of the liquid at the three-phase contact line. Bottom: Coordinate systems used. Dimensions are not to scale.

Normal Component of Liquid Surface Tension and Laplace Pressure.

A sitting liquid drop exerts a pressure, the Laplace pressure, to the surface of the solid plate. This pressure is

$$P = \frac{2\gamma}{R} = \frac{2\gamma \sin\Theta}{a} \qquad (26)$$

Here, ***R*** is the radius of curvature of the drop, ***a*** is the radius of the contact area, and Θ is the contact angle. At the rim of the drop, one has an additional force per unit length due to the surface tension of the liquid. The normal component of this force (per unit length) is directed upward and given by $\gamma' = \gamma \sin\Theta$. These forces cause a torque which is opposed by the elastic response of the cantilever. We divide the cantilever in infinitesimal thin stripes parallel to the ***Y*** axis (Fig. 12). At a given ***X*** position on the cantilever, the torque can be calculated. This torque is compensated by the restoring elastic response of the cantilever, which is described by $EI \cdot d^2Z/dX^2$, where ***I*** is the geometric moment of inertia and $I = wd^3/12$ for a cantilever with a rectangular cross section. By considering these two contributions the resulting inclination at the end of the drop ($X = a$) can be expressed as

$$\frac{dZ}{dX} = \frac{\pi a^3 \gamma \sin\Theta}{8EI} \qquad (27)$$

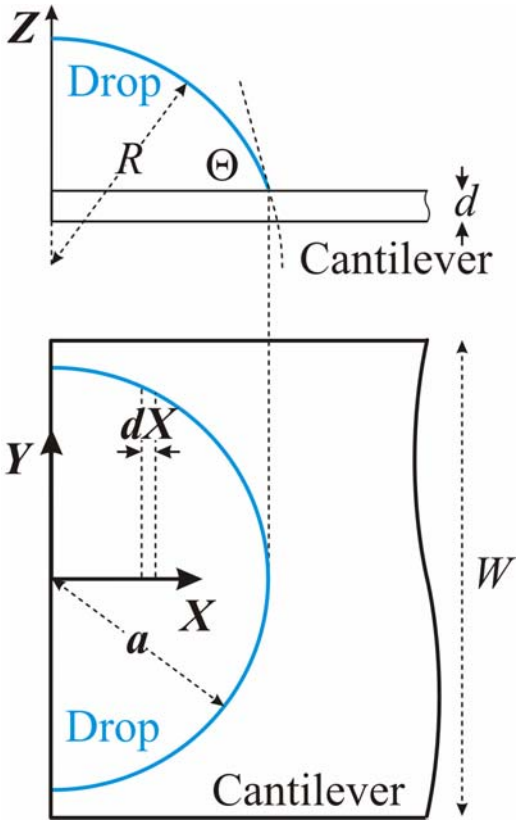

Figure 12. Side and top view schematics of a plate with a drop in its centre. Only one-half of the drop is shown.

The Laplace pressure and the normal component of the surface tension of the liquid are the dominant factors for cantilever bending [34, 35].

Change in Surface Stress.

Another contribution to the bending of the cantilever is the change in surface stress $\Delta\sigma$. In the contact area, solid/vapor surface is replaced by solid/liquid interface. This results in a change in surface stress and generates a constant torque over the whole contact area. Usually, the surface stress is reduced by a liquid, which leads to a bending away from the drop. If the whole surface of the cantilever would be covered, the bending would be described by Stoneys formula [76]. In my case, only the contact πa^2 area contributes and the inclination is given by

$$\frac{dZ}{dX} = -\frac{\pi\Delta\sigma a^2 d}{4EI} \qquad (28)$$

Lateral Component of Liquid Surface Tension.

The surface tension of the liquid also has a component parallel to the cantilever surface, which is $\gamma\cos\Theta$. This causes a contraction (for $\Theta < 90°$) or expansion (for $\Theta > 90°$) of the top surface and, thus, a bending of the cantilever. In this case the inclination at the drop end is

$$\frac{dZ}{dX} = \frac{\pi a^2 d\gamma \cos\Theta}{4EI} \tag{29}$$

In equilibrium, that is, if the three-phase contact line is not moving and line pinning is negligible, we can apply Young's equation, see Eq. (1). This leads to the conclusion that the lateral component should exactly compensate the effect of surface stress if $\Delta\sigma = \gamma_S - \gamma_{SL}$. The net effect of surface stress and the lateral component of the surface tension is thus for $X \geq a$

$$\frac{dZ}{dX} = \frac{\pi a^2 d}{4EI}(\gamma\cos\Theta - \Delta\sigma) \tag{30}$$

Only for small contact angles the combined effect of the lateral component of the liquid surface tension and the surface stress can possibly lead to a significant effect. This can be shown by dividing Eq.(30) by Eq. (27), and the result

$$\frac{d}{a}\bullet\frac{\cos\Theta - \Delta\sigma/\gamma}{\sin\Theta} \tag{31}$$

is usually much smaller than unity, because $d/a \ll 1$, unless the contact angle is small.

Line Tension.

If energy is required (released) to form the three-phase contact line, that effect tends to contract (expand) the periphery of the drop. At a given position X, the line tension κ contracts the top side of the cantilever with a certain force and the correspondent inclination induced by this force can be expressed as (for $X \geq a$)

$$\frac{dZ}{dX} = \frac{\pi a \kappa d}{4EI} \tag{32}$$

To estimate the effect of line tension, by dividing Eq. (32) by Eq. (27) we obtain

$$\frac{d}{a}\frac{2\kappa}{a\gamma\sin\Theta} \tag{33}$$

Unless the contact angle is small the effect of line tension is negligible because $\boldsymbol{d/a} \ll 1$ and $\boldsymbol{a\gamma}$ is on the order of 10^{-7} N, which is much larger than normal line tensions, which are below 10^{-8} N.

Effect of Gravitation.

The gravitational force due to the weight of the drop is small [77]. Even the largest drops ($\boldsymbol{R}$ = 30 μm) lead to a gravitational force of only 1.1 nN. A cantilever with K = 0.2 N/m is bent downward (negative deflection) at the end by 5.5 nm. The deflections discussed in this work are much larger, and gravitation is thus neglected.

Considering all the Contributions for the Cantilever.

Until now, all results were given in the coordinate system ***XYZ*** which originates in the center of the contact area of the drop. In the coordinate system *xyz*, $\boldsymbol{x}$ is parallel to the cantilever at its base and oriented horizontally. The drop is centered at $\boldsymbol{x_0}$. For $\boldsymbol{x} \le \boldsymbol{x_0} - \boldsymbol{a}$, deflection and inclination are zero ($dz/dx = 0$, z=0). For $\boldsymbol{x} \ge \boldsymbol{x_0} + \boldsymbol{a}$, the inclination is given by twice dZ/dX, leading to

$$\frac{dz}{dx} = \frac{\pi a^3}{4EI}\left[\gamma\sin\Theta + \frac{2d}{a}\left(\gamma\cos\Theta - \Delta\sigma + \frac{\kappa}{a}\right)\right] \tag{34}$$

Here, *z(x)* describes the shape of the cantilever. The first term is caused by the Laplace pressure and the normal component of the liquid surface tension. It leads to an upward bending of the cantilever toward the drop. The second term disappears for $\boldsymbol{\Delta\sigma = \gamma_S - \gamma_{SL}}$, that is, when Young's equation is valid and the difference in the solid surface tensions is equal to the change in surface stress. The last term is expected to be small, so that one can approximately write for $\boldsymbol{x} \ge \boldsymbol{x_0} + \boldsymbol{a}$

$$\frac{dz}{dx} \approx \frac{\pi a^3}{4EI}\gamma\sin\Theta \tag{35}$$

Inclination and Deflection of the Cantilever.

In commercial AFMs, as well as in my experimental setup (see Chapter 2) the inclination at the end of the cantilever is measured by the optical lever technique. Inclination is usually converted to deflection by pushing the end of the cantilever upward by a defined distance. If one applies a force at its end, the shape of the cantilever is described by a third-order polynomial. Deflection $z(l_0)$ and inclination dz/dx ($\boldsymbol{x} = \boldsymbol{l_0}$) are related by [78]

$$\frac{dz}{dx}(l_0) = \frac{3}{2l_0} z(l_0) \qquad (36)$$

An example is shown to demonstrate that at the same deflection $z(l_0)$ caused by a concentrated force applied at the end of the cantilever or by a drop in the middle of the cantilever the inclination dz/dx ($\boldsymbol{x} = \boldsymbol{l_0}$) is different (Fig. 13). The deflection caused by a given force can be calculated with $z=F/(2EI)(l_0x^2-x^3/3)$, [75]. The force was chosen so that the resulting deflection is similar to the one caused by the drop. The parameters to calculate the effect of the drop were d=1 μm, w=100 μm, a=40 μm, and $\Theta=30^o$. The length of the cantilever was assumed to be l_0=400 μm. The center of the drop is placed x_0=60 μm away from the base [34].

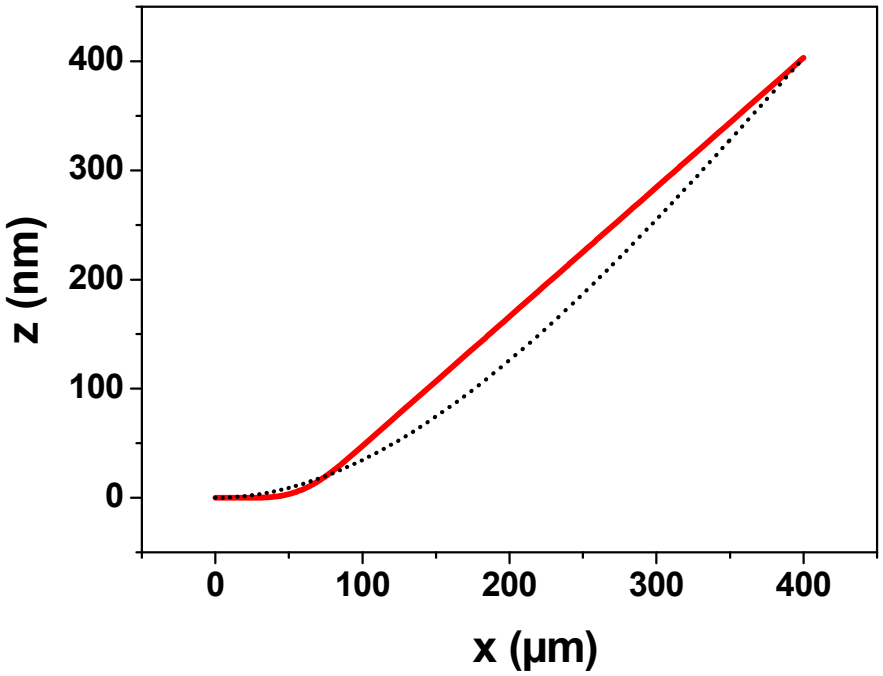

Figure 13. Comparison of a cantilever deflected by a drop on top (red line) and a cantilever deflected by a force of F=28 nN at its end (dashed line).

Chapter 2

Materials and Methods

2.1 Instrumentation

The first step of my work was to develop and set up a modified AFM-related Reversed Particle Interaction Apparatus [34, 41, 79, 80], which was used for both cantilever spring constant calibration and drop evaporation experiments. The setup consists of three main units. The first one is the R-PIA itself with some simplifications, the second one is the commercially available piezoelectric drop generator, and the third one visualizes the processes of drop deposition and evaporation by means of standard video microscopy. The piezoelectric drop generator and the R-PIA are synchronized and operated via a fully computer controlled self-developed software.

2.1.1 Reversed Particle Interaction Apparatus

Figure 14 shows the scheme of the Reversed Particle Interaction Apparatus. There are five main differences compared with the PIA [79] to be mentioned:

- The whole setup is placed upside down for easy drop deposition by the ink-jet dispenser, which is located directly above cantilever.
- The cantilever holder is easily accessible for modifications.
- R-PIA is equipped with only one piezo movable vertically with 12 μ-meter range, which is used for the calibration purpose only (see below).
- A laser, a cantilever holder, a mirror and Position Sensitive Device (PSD) are coupled to the piezo through the frame so that the setup is capable of moving in vertical direction as a whole keeping laser pathway configuration constant and thus allowing for its calibration.

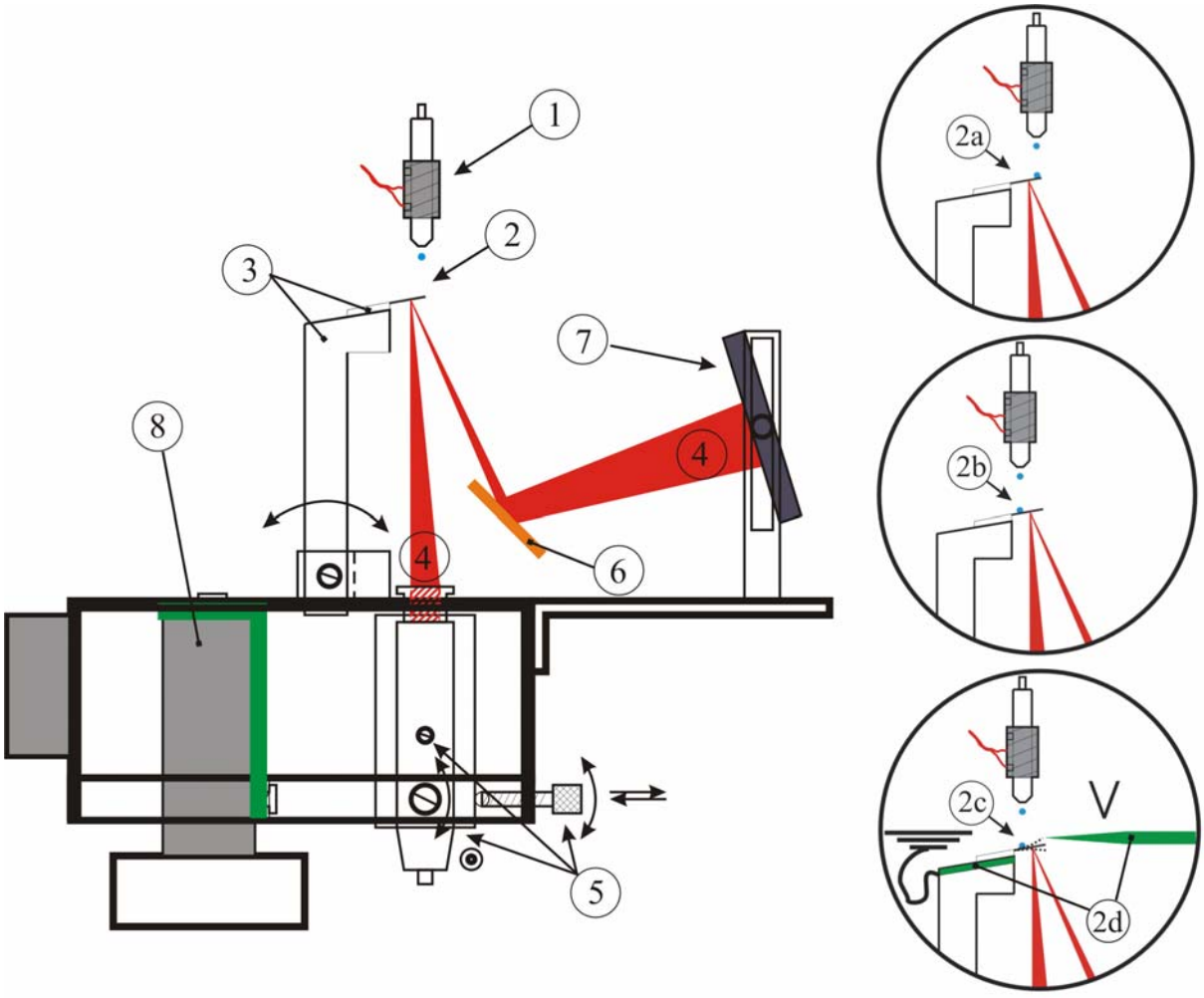

Figure 14. R-PIA (Reversed Particle Interaction Apparatus) indicating (1) piezoelectric drop generator (see also Figure 16), (2) a cantilever with (3) its holder, (4) a 5 mW and 670 nm laser light source, (5) adjusting fine screws for precise positioning of the laser spot on the backside of the cantilever, (6) a mirror, (7) PSD for monitoring the cantilever deflection, (8) a calibrating piezo for vertical displacements. Three insets indicate correspondent regimes of R-PIA use, (2a) for cantilever spring constant calibration; for monitoring drop evaporation by sensing the cantilever inclination (2b); for monitoring of drop evaporation by sensing the change in resonance frequency (2c); a grounded cantilever to be excited with periodic electric impulses by a needle with an applied potential (2d). The camera with the zoom optics is directed perpendicularly to the plane of the figure.

- Before or after an experiment each cantilever – reflected laser pathway configuration must be calibrated to obtain the V/nm (Volts per nanometer) ratio. It can be done pushing a free end of an under-test cantilever towards a reference surface, which can be the planar area of the droplet generator capillary edge.

The chip is clamped to a holder made of PEEK, and the upper side of the cantilever(s) faces the orifice of the drop generator. The holder is mounted on the base, which is a solid frame for hosting the light lever technique components. The circular laser spot in diameter with 50 μm or less is focused on the backside of the cantilever. The spot is adjusted in the centre of the cantilever with fine x- and y-screws (OWIS GmbH, Germany). By using a two-dimensional PSD the movements of the reflected laser beam are monitored. The PSD provides two output currents, which are converted to the voltages U_V and U_H. These two voltages are proportional to the position of the laser spot with respect to the vertical and horizontal direction. Both voltages range from -10 V to +10 V. The PSD has an active area of 20×20 mm^2, in order to have a large dynamic range.

The control software starts acquiring cantilever inclination data in order to define the baseline for zero inclination. Then a drop of water is ejected from the capillary nozzle and is deposited in the middle of the cantilever. Simultaneously, the cantilever is excited by periodic electric impulses applied at its end by a sharp tungsten needle (spherical curvature of about 2 μm). The silicon cantilever is grounded. In response to the periodically applied electrostatic field the cantilever is excited, while bearing an evaporating drop on it. The inclination data is read out by the software until completion of drop evaporation.

A typical example of an experimental signal is shown in Fig. 15. The signal is filtered through a bandwidth filter to reduce noise and to remove frequencies of higher oscillation modes. Blue hollow circles represent the time when an electric impulse of duration 100 μs and potential of 100 V is applied. Being excited the cantilever starts to oscillate. As a result, amplified cantilever thermal vibrations are resolved mostly in the first mode and are dampened within 3 ms. By taking a time difference within a certain amount of single vibrations and dividing it by the number of periods inside the chosen time domain, a reversed value of resonance frequency can be obtained. The choice of the electric impulse duration and its amplitude to obtain the best signal/noise ratio depends on the cantilever properties and on the desired resolution, which can go down to 1 ms in time and 50 pg in mass. The equation is

$$\Delta m = \frac{K(f_i^2 - f_j^2)}{4\pi^2 f_i^2 f_j^2} \qquad (37)$$

where Δm is a change in mass, f_i and f_j are frequencies at times t_i and t_j ($t_i<t_j$). The spring constant of the cantilever K can be determined ***in situ*** since the initial drop mass is known from video images

and the frequency is recorded (see Chapter 3.1). The unfiltered signal contains also information on the cantilever bending, that is when the vibrations are completely dampened.

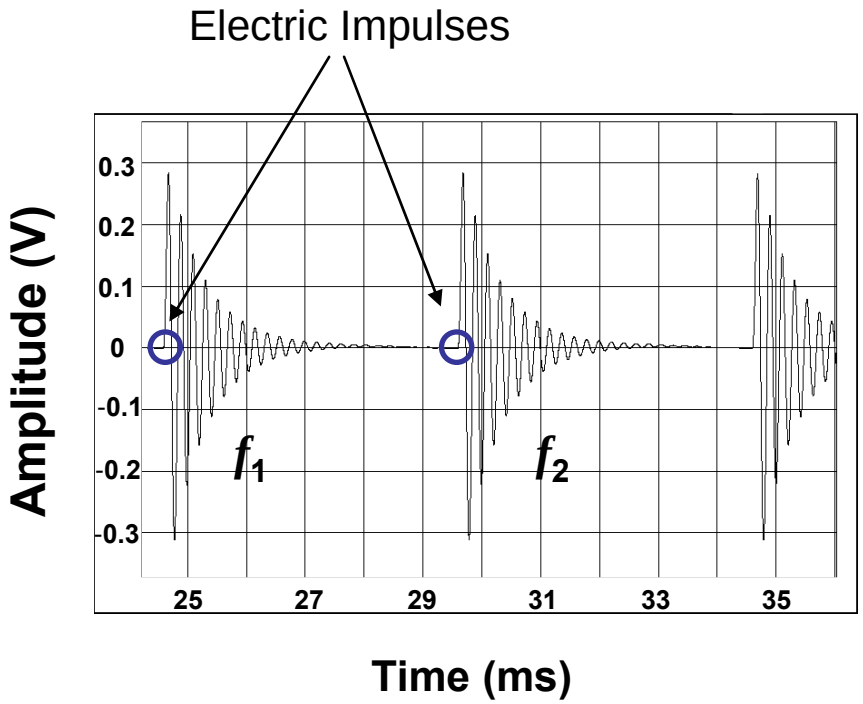

Figure 15. Example of a typical experimental signal passed through a bandwidth filter: amplitude vs. time. Within each 5 ms period (as an example) the free end of the cantilever is excited by an electric impulse of typically 100 μs seconds. The frequencies f_1 and f_2 of the dampened oscillations are determined. The inclination of the cantilever is recorded before filtering the signal.

To visualize drop deposition and evaporation processes, the position, and the contours of the drops are monitored with a camera system consisting of an objective 5× (Mitutoyo Corp., Kawasaki, Japan), a 6.5× Ultra zoom tube (Navitar Inc., Rochester, NY), and a uEye UI-2210-C, charge coupled device (CCD) camera (IDS GmbH, Obersulm, Germany), together with a white light source (Schott KL 1500, Mainz, Germany). The resolution of a single frame was 640×480 pixels; the frame rate varied from 18 to 30 fps (frames per second). From video images, contact radius *a* and height *h* of the drops, as well as their distance *l* from the fixed end of the cantilever were obtained. To know the μm/pixel ratio the system was calibrated using a cantilever with a known length. From *a* and *h*, the drop volume and the contact angle for each image were calculated by using Eqs. (6) and (7). The drop deposition experiments took place at a temperature of 21±1 °C and a relative humidity of 40±5% (SHT15, Sensirion, www.sensirion.ch).

2.1.2 Regimes of R-PIA operation

R-PIA can be used in three different regimes developed and used in this work.

- ***Cantilever Spring Constant Calibration using Microdrops***

  The first regime of operation is to use R-PIA for calibrating the spring constant of cantilevers. The laser is focused near the base of a cantilever or on one of its arms if a triangular cantilever is calibrated. The spring constant is found by measuring the resonance frequency of the unloaded cantilever and of the cantilever loaded with a drop with known mass.

- ***Microdrop Evaporation sensed by Cantilever Inclination***

  In this regime the optical lever technique detects cantilever responses not only to drop impact, but also to surface tension. These effects act at the drop rim and within its cap area and change during drop evaporation [34].

- ***Microdrop Evaporation sensed by Cantilever Resonance Frequency and Inclination***

  A novel method was developed, by means of which I monitored the resonance frequency and the cantilever inclination simultaneously during drop evaporation. Thus, two independent signals can be measured by using one cantilever.

2.1.3 Piezoelectric Drop Generator

The R-PIA is equipped with a commercially available ink-jet dispenser – Piezoelectric Drop Generator (PEDG) (Piezodropper, Universität Bremen, Germany)[81]. For its construction details, see Figure 16. The PEDG can be operated in two modes: ***Continuous-Jet-Mode*** and ***Drop-On-Demand-Mode***. In the Continuous-Jet-Mode a continuous jet will disintegrate into monosized droplets. In the Drop-On-Demand-Mode a single droplet is produced. The droplet diameter is approximately double the diameter of the nozzle in the Continuous-Jet-Mode, and can be smaller than a half of the nozzle diameter in the Drop-On-Demand-Mode. We operated the device in the Drop-On-Demand-Mode. The velocity of the droplets is about 2 m/s. During my work I used a nozzle with an aperture diameter of 45 μm, and drop radii varied between 15-45 μm. By variation of the parameters like frequency, impulse duration and voltage, drops of different diameters can be

produced. The drop size also depends on the specific liquid used. Drops of different liquids with viscosities smaller than 100 mPa*s can be generated.

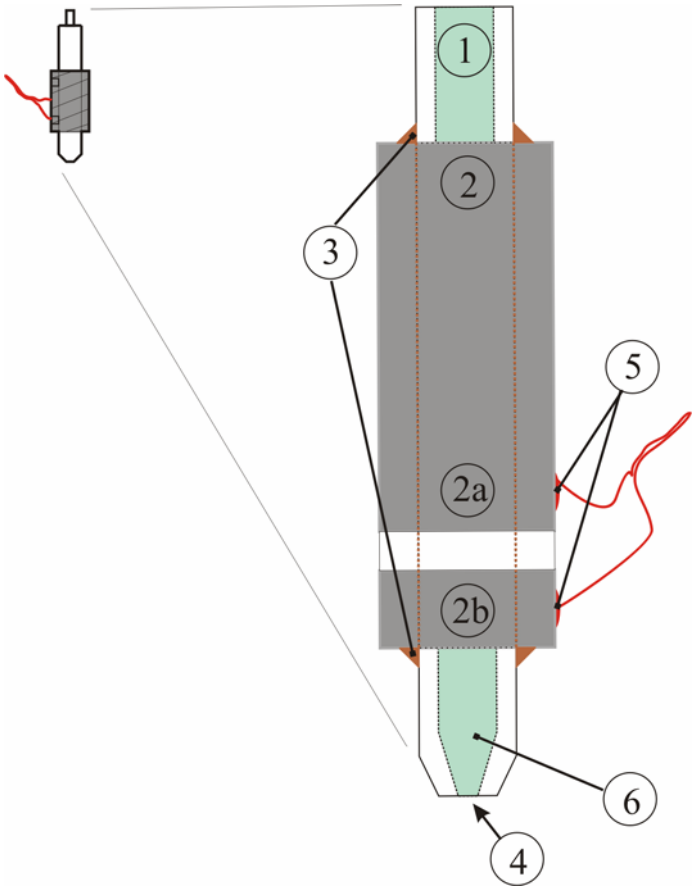

Figure 16. PEDG (piezoelectric drop generator) indicating (1) boron silicate glass capillary embedded into (2) a piezo tube consisting of two separated aluminium (2a) outer and (2b) inner electrodes. The piezo tube is fixed on the capillary by (3) epoxy glue on both sides and in between. (6) A liquid drop is ejected through (4) the capillary orifice, when a voltage is applied to (5) the piezo contacts.

A three-axis, electromotor-controlled micromanipulator (Luigs & Neumann GmbH, Ratingen, Germany) was used for depositing drops on the desired place on a horizontally mounted cantilever. The drop shape was analyzed automatically with a home made software. The distance between nozzle and cantilever was always below 0.2 mm.

Both R-PIA and PEDG are fully controlled by a personal computer and their operational functions are synchronized. The self-written software, developed in LabView (National Instruments Corp., Austin, USA), consists of a real-time panel containing controls for the drop generator and data acquisition timing. Data saving and calibration tasks are also included. An electric impulse being an output signal to the drop generator piezo triggers input channels of PSD to be read out. D/A and A/D conversions are operated by two PCI board cards. The PCI-6711 board controls PEDG and the PCI-

6251 board (both boards are from National Instruments Corp.) controls R-PIA with 16-bit resolution for both input and output.

2.1.4 Experiments in Saturated Atmosphere

To study the evaporation process of small water drops in saturated atmosphere a specially constructed glass cell was used [46] (Fig. 17). Small drops were deposited onto hydrophobized silicon cantilevers (the cantilevers and hydrophobization procedure are described below). Cantilevers were only 90 μm wide so that the optical axis could be aligned with the plane of the cantilever. To create a saturated water vapor atmosphere in a closed system we used a glass container (5×5 cm^2 base area, 1 cm high) covered at the top by Parafilm (Alcan Inc., Neehan, WI, USA).

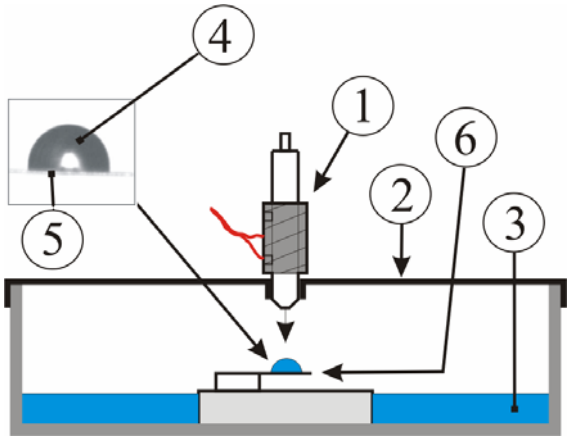

Figure 17. Experimental setup – a glass cell – used to study evaporation of water drops in saturated water vapor atmosphere. (1) PEDG, (2) parafilm, (3) water, (4) water drop on (5) hydrophobized silicon cantilever, (6) evaporating drop.

The substrate was lifted ≈1 mm above a thin layer of water (deposited before the glass chamber is closed) at the bottom of the container. A large drop of ≈ 2 mm radius of curvature was placed directly underneath the cantilever. The nozzle of the drop generator was pushed through the Parafilm to a distance of ≈0.2 mm above the cantilever. Drops of different radii (15-36 μm) and thus volumina (14000-195000 μm^3) were produced. Before performing the experiments in a closed system in the presence of water a level of relative humidity (RH) was measured with a humidity sensor (SHT15, Sensirion, www.sensirion.ch) with an accuracy of 2% specified in the range 10-90%. The RH was found to be 99 %.

2.2 Cantilevers

Rectangular silicon cantilevers from Nanosensors, Neuchatel, Switzerland and Micromotive GmbH, Mainz, Germany together with triangular silicon nitride cantilevers from Veeco Instruments, Santa Barbara, CA were used for the spring constant calibration. To study drop evaporation I used micromachined silicon rectangular cantilevers of 90 μm width and about 1 μm thick from Micromotive GmbH. SEM pictures of all mentioned types of cantilevers are shown in Fig. 18. Beside the dimensions of a cantilever, its mechanical properties mainly depend on material density ρ, Young's modulus E, and Poisson's ratio ν. Silicon has ρ=2330 kg/m^3, E=180 GPa, ν=0.26, and silicon nitride has ρ=3100 kg/m^3, E= 210 GPa, and ν=0.24.

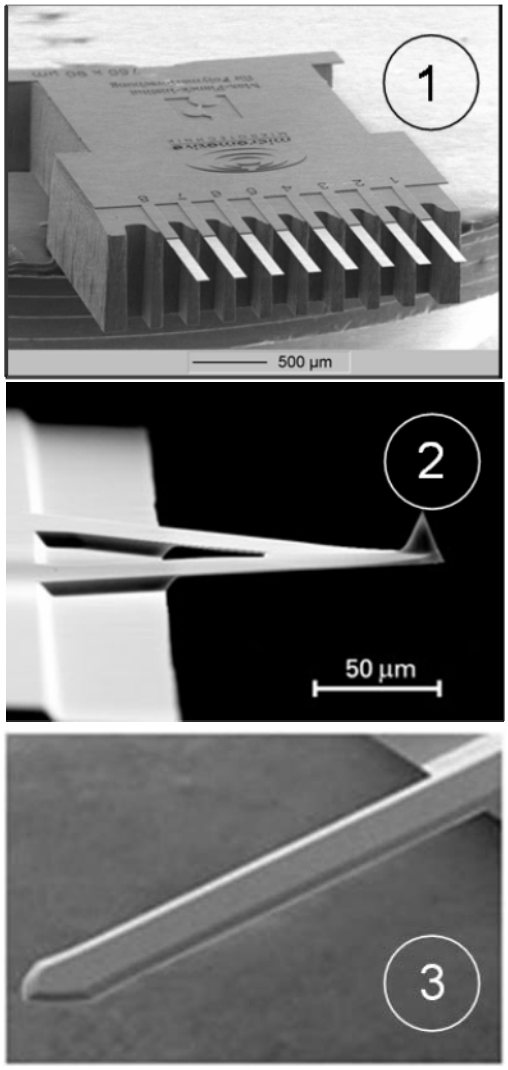

Figure 18. SEM images of cantilevers of different types. (1) A chip with 8 silicon cantilevers – micromechanical sensors ("octosensis"); (2) a triangular silicon nitride cantilever from www.spmtips.com; (3) a rectangular tipless cantilever from www.nanosensors.com.

2.3 Chemicals and Cantilever Surface Preparation

Liquids. Water (milliQ, Millipore Corp., USA.) and methanol, ethanol, propanol, butanol, pentanol, hexanol, and octanol all of p.A. purity are used.

Hydrophobic "octosensis" cantilevers were prepared according to the following two procedures:

- Perfluoro-1,3-dimethylcyclohexane (Aldrich, 80% technical quality isomeric mixture) was deposited on cantilevers by plasma polymerization [82] to form a hydrophobic film on the surface. The thickness of the perfluorocarbon film was measured by ellipsometry and found to be (50±3) nm.
- Cantilevers were treated in O_2 plasma ($PlasmaPrep_2$, GaLa Instrumente, Germany) for 100 s and then hydrophobized by exposing them to a vapor of 1,1,1,3,3,3-hexamethyldisilazane (Aldrich, Germany, 99.9%) for 5 h at 70 °C.

Gold coated "octosensis" cantilevers were prepared as described below:
Cantilevers were coated uniformly by gold by a standard metal evaporation method. The cantilevers were etched in Ar-plasma for 10 minutes at $1.6 \cdot 10^{-2}$ mbar before gold evaporation. For a better adhesion of the 30 nm thick gold layer to the silicon surface of the cantilevers a 3 nm chromium Cr layer was deposited prior gold deposition. Both types of cantilevers ("gold-on-top" and "gold-on-bottom") were coated simultaneously, thus obtaining equal thicknesses of the Cr and Au layers.

2.4 Cantilever Calibration

A number of methods for the calibration of the spring constant of AFM cantilevers exist. At least four calibration methods have taken root, and they are described in a series of reviews [83-85]. The first method is proposed by Sader et al [86-90] and is based on geometric and material properties of the cantilever (dimensions, density, and Young's modulus) together with the experimentally measured resonance frequency and quality factor, plus the viscosity and density of the medium in which the cantilever is immersed. This approach is suitable for rectangular cantilevers, whose dimensions are known, and shows good results (std. dev. <10%). The second method is more precise and based on the acquisition of the cantilever's thermal noise (**TN**) spectrum [74, 91]. It can be used for any type of cantilevers, but it is affected by one drawback: at least one force-distance curve

against a hard surface has to be acquired in order to calibrate the spectrum. This often causes damage and/or contamination to the tip of the cantilever. The third method represents so-called direct techniques, where known forces are applied to the cantilever: these might be a known hydrodynamic drag at the end of the cantilever [92-94] or along it [95], the loading with a second cantilever of known force constant [96], the exertion of a known electrostatic force [97], and the bombardment with drops of known mass and velocity [34, 35]. In nearly all these cases a specially developed instrument is required. One also should take into account that contamination and damage of the tip can most likely occur during the calibration while pressing the cantilever towards a reference surface. The fourth method, and the most cited/used according to ISI-Web of Science^{SM}, which allows for an absolute and extremely precise calibration was proposed by Cleveland *et al* [40]. The idea is to measure the shift of the resonance frequency of a cantilever after loading it at its end with small, known masses. This technique, called added-mass method, works with all types of cantilevers and suffers from no restrictions, except that the mass must be placed at the very end of the cantilever and that it is time demanding.

- Different particles with known mass or density must be carefully positioned onto the cantilever without contaminating it or damaging its tip;
- the thermal noise spectrum has to be recorded for each particle;
- the particles must be removed, without damaging the cantilever, and placed onto a sample holder; and
- must be later characterized in an electron microscope.

The technique would profit if some of the steps could be simplified or shortened. Motivated by this issue I have looked for a potential extension to this long established method, and I have used water microdrops instead of particles to load cantilevers with small masses (Fig. 19)[34, 98]. The technique by means of which water drops are deposited was described above (see Chapter 2.1.2). The results of this method are presented and discussed in detail in Chapter 3. The thermal noise (**TN**) method was used in this work to determine spring constants $\boldsymbol{K_{TN}}$ of cantilevers to be later compared with those measured by using water microdrops. For drop evaporation experiments the cantilever spring constant can be determined ***in situ***, with obvious advantages.

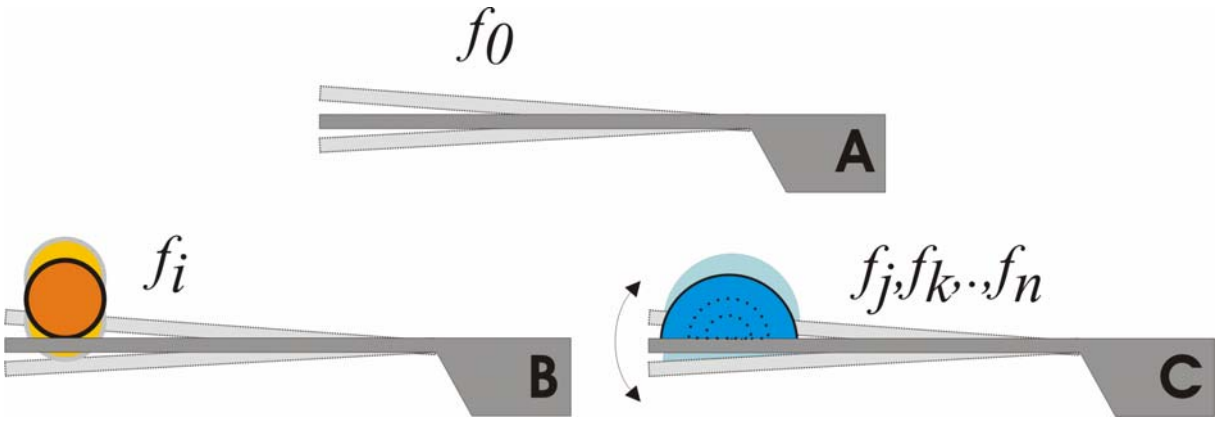

Figure 19. The added mass method to determine the spring constant of a cantilever (A) using solid particles of different masses (B), and using water microdrops of different sizes.

2.5 Drop-On-Cantilever Simulations

2.5.1. Spring Constant of a Cantilever

It is not possible to find an analytic solution for the equation of motion of a cantilever with a drop deposited at an arbitrary position along its length axis different from the very end (see Chapter 1). And for larger "drop – cantilever end" distances Eq. (25) is not valid. The alternative is to use numerical simulations. To this purpose, a numerical three dimensional (3D) model is implemented and solved by means of the FEM software package COMSOL Multiphysics by our collaboration partners [35, 99]. This model, contrary to beam theory, takes into account Poisson's ratio ν of the cantilever material [35], which for silicon is around 0.26. For reasons of simplicity instead of a spherical drop an equivalent cylindrical drop having similar mass is used (Fig. 20). Surface tension effects are also not considered. The dimensions of the cylinder are calculated from the drop mass $\boldsymbol{m}$ and the contact radius $\boldsymbol{a}$, which are known from video analysis. The radius of the cylinder $\boldsymbol{a_{cyl}}$ is set equal to the contact radius of the drop and calculated the height $\boldsymbol{h_{cyl}}$ by

$$h_{cyl} = \frac{m}{a_{cyl}\rho_d \pi} \tag{38}$$

with ρ_d the density of the drop. The center of mass of cylinder and drop are the same. The cantilever with its known material properties ($\boldsymbol{E}$, $\boldsymbol{\nu}$, and $\boldsymbol{\rho}$) and dimensions ($\boldsymbol{l_0}$, $\boldsymbol{w}$, and $\boldsymbol{d}$) is modeled as a cuboid clamped on one side. The simulation typically comprises about 10.000 elements and about 60.000 degrees of freedom using an unstructured tetrahedron mesh. In order to improve the numerical

accuracy the initial mesh was automatically refined two times. The model was validated by comparing the simulated resonance frequencies of the loaded as well as of the unloaded cantilevers with the resonance frequencies

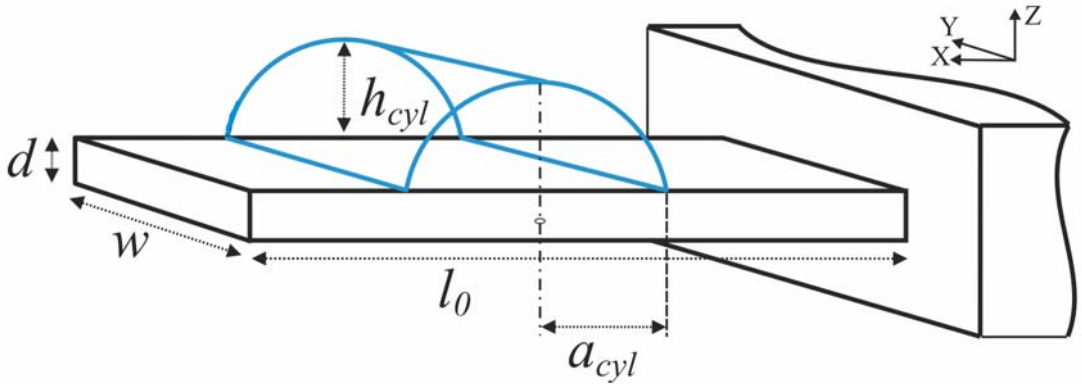

Figure 20. Sketch representing a cylindrical drop on a cantilever used in 3D FEM simulation model with related nomenclature.

measured in the experiments. With this so called "forward simulation" we can confirm the experimental method, i.e., calculate the resonance frequency using parameters of the cantilever (***E***, ***ν***, ***ρ***, $\boldsymbol{l_0}$, ***w***, and ***d***) known *a priori*. On the other hand, one could use an "inverse simulation" to determine unknown parameters which are experimentally hardly accessible. We could thus solve the inverse problem of identifying the cantilever's thickness with respect to a given resonance frequency $\boldsymbol{f_i}$ by inserting the other parameters (***E***, ***ν***, ***ρ***, $\boldsymbol{l_0}$, ***w***, and $\boldsymbol{f_i}$) into an optimization routine for obtaining the thickness by minimizing the error between simulated and measured resonance frequencies. The optimization routine is stopped when the error is below 0.1%. The inverse problem is solved for the unloaded cantilever and for each configuration where a drop is sitting at a different position along the cantilever. Then the mean value of all obtained thicknesses is inserted into Eq. (18) to calculate the spring constant of the cantilever.

2.5.2. Evaporative Cooling Effect

When a drop of water evaporates from a cantilever coated by gold its bending caused by surface tension effects (see Eq. 35) is significantly altered by the cooling of the evaporating drop due to the difference of gold and silicon thermal expansion coefficients (see Chapter 1). Unfortunately, it is not possible to separate these two effects experimentally. For the purpose of their separation and quantification 3D FEM simulations were implemented in Ansys Pro by our collaboration partners. The simulation model described above for the cantilever spring constant evaluation is valid for this

case also, but with two main differences. First, a normal spherical drop at the cantilever's fixed end is considered (Fig. 21), thus, surface tension effects are taken into account. Second, the model is upgraded with thin layered thermal shell elements accounting on thermal fluxes and convection/radiation boundary conditions. For the simulations following parameters enter the model, besides the above mentioned cantilever properties: drop cap radius $\boldsymbol{a}$ and contact angle Θ, distance of a drop center $\boldsymbol{l_{drop}}$ from the base of the cantilever, thickness of the gold layer $\boldsymbol{d_{gold}}$, Poisson's ratios for silicon (ν_{Si}=0.26) and gold (ν_{Au}=0.44) as well as their thermal linear expansion coefficients α_{Si}=2.6 μm/mK and α_{Au}=17.6 μm/mK. Gold has a Young's modulus $\mathbf{E_{Au}}$= 73 GPa. This model computes cantilever deflections for both the surface tension and the cooling effects separately. In order to obtain an inclination comparable with the experimental one, the two contributions are added.

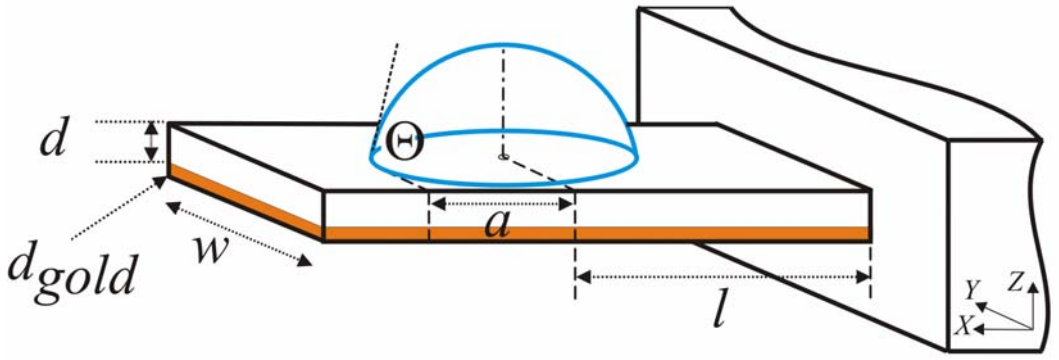

Figure 21. 3D FEM model used for simulations of the cantilever inclination caused by both the surface tension effects and the evaporative cooling.

Chapter 3

Results and Discussions

In this chapter, I describe the results of two kinds of measurements can take place depending on the drop location along cantilever as well as on a chosen time domain to work with (the drop deposition or the drop evaporation [34]). First, water microdrops can be utilized as convenient loading substituents of attached particles in Cleveland method for cantilever calibration. Second, the evaporation of microdrops of water or other liquids can be sensitively traced by a cantilever. Herein I present the following results on:

- ***Cantilever spring constant calibration using water microdrops.*** For the spring constant calibration of cantilevers two paths are developed [41]: Constant Drop Location and Constant Drop Mass regimes. In the first regime drops of different masses are deposited at the end of a cantilever while in the second one drops of similar mass are placed along the cantilever length axis. The last regime needs to use finite element method simulations (see Chapter 2).

Four different aspects take place during drop evaporation:

- ***Type of Liquid and Surface Tension.*** Evaporation of water and low molecular weight normal alcohols from a hydrophobic surface is investigated by measuring cantilever inclinations. Modes of evaporation are analyzed. The role of the surface tension and the specific dependence of the cantilever overbending on the molecular weight of the alcohols are discussed.

- ***Evaporative Cooling*** is examined by depositing water drops on thermosensitive cantilevers with a gold layer on either top or bottom sides. Upward (gold layer on top) or downward (gold layer on bottom) bendings are then compared with one measured on a bare silicon cantilever and are quantified by FEM simulations.

- ***Surface Stress caused by Drop Evaporation***. A novel technique allowing for simultaneous inclination and frequency measurements of a cantilever loaded by a drop is introduced. The technique is validated in the case of a microdrop on a hydrophobic cantilever surface. Video microscopy drop data and data obtained from the cantilever inclination and the resonance frequency are compared. With the new method an effect arising with pinned microdrops on hydrophilic surface – cantilever "overbending", i. e. negative inclination, – is measured and quantitatively evaluated for the first time. A tentative explanation why cantilever bends downwards at the end of drop evaporation is suggested by considering change in the surface stress towards the end of the drop evaporation.

- The results on ***nonequilibrium effects for small drops*** in water vapor saturated atmosphere are presented and discussed in terms of the recently proposed strict thermodynamic derivation of time constants for drop evaporation [46].

3.1 Cantilever Spring Constant Calibration using Water Microdrops

By looking for an alternative to Cleveland's spring constant calibration method, I have used water microdrops instead of particles to load cantilevers with small masses. Two advantages are expected from this approach: first, I avoid contamination by working "contactless", in the sense that I shoot a water drop onto the cantilever from a certain distance using an inkjet dispenser; second, since the drop evaporates after some seconds, I do not need to remove the mass "by hand" [40].
I pursue two paths to verify the validity of the technique. First, I deposit microdrops with different sizes at the cantilever end (Constant Drop Location), which is similar to the added-mass method, and compare the results with the predictions from beam theory. Second, I deposit microdrops of equal sizes at different positions along the cantilever (Constant Drop Mass) and compare the results with the predictions of FEM simulations.

3.1.1 Constant Drop Location

A typical experimental cantilever deflection versus time curve after drop impact and a fit of the curve with Eq. (20) are shown in Figure 22. The cantilever is at rest for $t<0$, it is excited at $t=0$ and starts to oscillate, and it is damped for $t>0$ until the resting position is again attained.

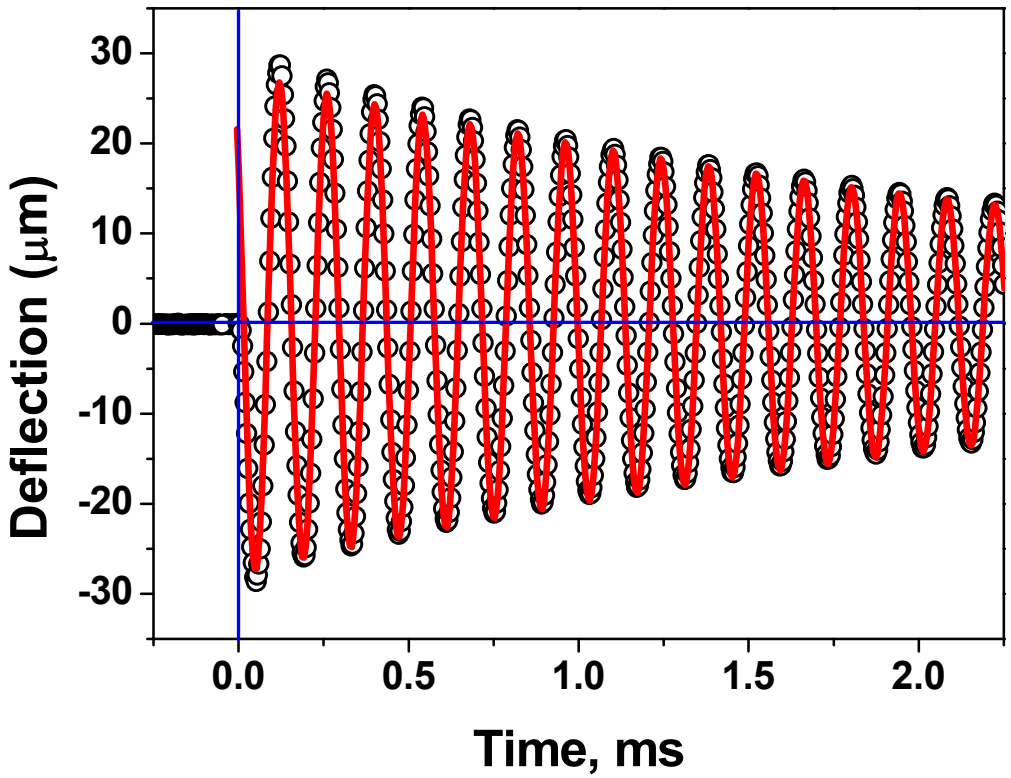

Figure 22. Cantilever deflection vs. time after drop impact. Drop properties: initial mass m_i=68.3 ng, R=25.37 μm, velocity ν_0=2.2 m/s. Cantilever properties: l_0=500 μm, w=90 μm, d=1.89 μm. Negative deflection indicates that the cantilever is bent downward. Open circles (O) represent the oscillating cantilever deflection. The solid line represents a fit of Eq. (20) to experimental data points (A_0=27.9 mm, f_i=7114 Hz, τ_d=2.98 ms).

I performed three series of experiments using different cantilevers and drops (see also Table I at the end of this paragraph):

(**A**) Rectangular Micromotive cantilever with f_0 =10 404 Hz and K_{TN}=0.19±0.01 N/m, seven drops, masses varied from 44.2 ng (R=21.95 μm) to 135.4 ng (R=31.88 μm).

B) Rectangular Nanosensors cantilever with f_0 =11 782 Hz and K_{TN}=0.13±0.01 N/m, seven drops, masses varied from 43.1 ng (R=21.76 μm) to 135.5 ng (R=31.88 μm).
(**C**) Triangular Veeco cantilever with f_0=19 253 Hz and K_{TN}=0.10±0.01 N/m, three drops, masses varied from 1.1 ng (R=6.41 μm) to 53.7 ng (R=23.41 μm).

According to Eq. (24), which establishes the relation between the deposited mass and the resulting resonance frequency of the cantilever, the results of the three series of measurements are shown in Fig. 23. The unloaded resonance frequencies of cantilevers are also included in the data sets ($\boldsymbol{m}$=0). The relation between the drop mass $\boldsymbol{m}$ and $1/(2\pi f)^2$ is linear, as expected. A linear regression of the data yields effective mass and the slopes of the fitted lines provide the spring constants:

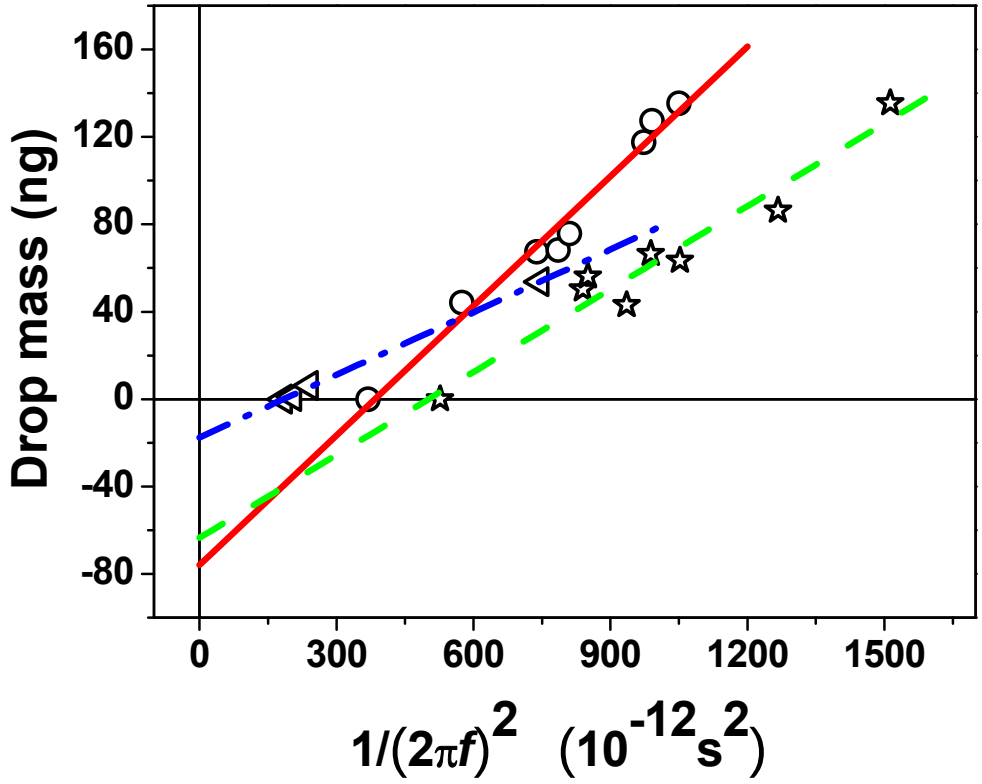

Figure 23. Plots of different water drop masses vs. 1/ $(2\pi f)^2$ according to Eq. (24) for three cantilevers. (A) Rectangular cantilever: l_0=500 μm, w=90 μm, m_{eff}=75.9 ng, K=0.198±0.012 N/m. (B) Rectangular cantilever: l_0=460 μm, w=50 μm, m_{eff}=63.4 ng, K=0.126±0.012 N/m. (C) Triangular cantilever: l_0=200 μm, w=22 μm, m_{eff}=17.6 ng, K=0.096±0.002 N/m.

$K_{exp(A)}$=0.198±0.012 N/m, $K_{exp(B)}$=0.126±0.012 N/m, and $K_{exp(C)}$ =0.096±0.002 N/m.

All these values differ by less than 5% from the values obtained by the TN method and confirm the validity of the technique. Moreover, no residues are left on the cantilever, which means that the AFM probe has not been corrupted or contaminated during calibration.

3.1.2 Constant Drop Mass

Drop sizes can be varied by the piezocontrol parameters, but this is time demanding: the drop size strongly depends on the inner diameter of the nozzle, which is fixed, and operating on the piezocontrols allows us to vary the drop diameter by at most an order of magnitude. This does provide only a limited spectrum of masses to be used for calibration. An alternative to changing drop sizes is to use the inkjet dispenser for generating monodisperse droplets (according to the manufacturer, the standard deviation of the drop diameters is less than 1%), and to deposit them at different positions along the length axis of the cantilever. Other than the previous technique, this is applicable only to rectangular cantilevers. The loads sensed by the cantilever are different, and so will be the shifts of the resonance frequencies with respect to the unloaded cantilever. Results of such experiments are presented in Fig. 24: drops of similar mass were deposited on three rectangular silicon cantilevers, all having the same width and only slightly different thicknesses, but distinct lengths and thus resonance frequencies. The spring constants are determined by the TN method, and the average thickness d of the cantilevers with Eq. (18). The parameters for all six cantilevers and calibration results are summarized in Table I.

(**D**) l_0=297 μm, K_{TN}=0.178±0.01 N/m, d=1.05 μm.
(**E**) l_0=372 μm, K_{TN} =0.104±0.01 N/m, d=1.09 μm
(**F**) l_0=503 μm, K_{TN} =0.053±0.003 N/m, d=1.18 μm

For each cantilever I performed two series of experiments, each one with a different load (54 experimental configurations in total). In fact, drops of different masses located at the same position cause different frequency shifts, as is demonstrated, e.g., by drops 3 and 4. Furthermore, an evaluation of the curves in Fig. 24 confirms what was mentioned before, i.e., that the relationship between drop position and resonance frequency is not linear. Since it is not possible to find an analytic solution analog to Eq. (17) for these types of “cantilever-mass” configuration, we had to simulate them (continuous lines in Fig. 24).

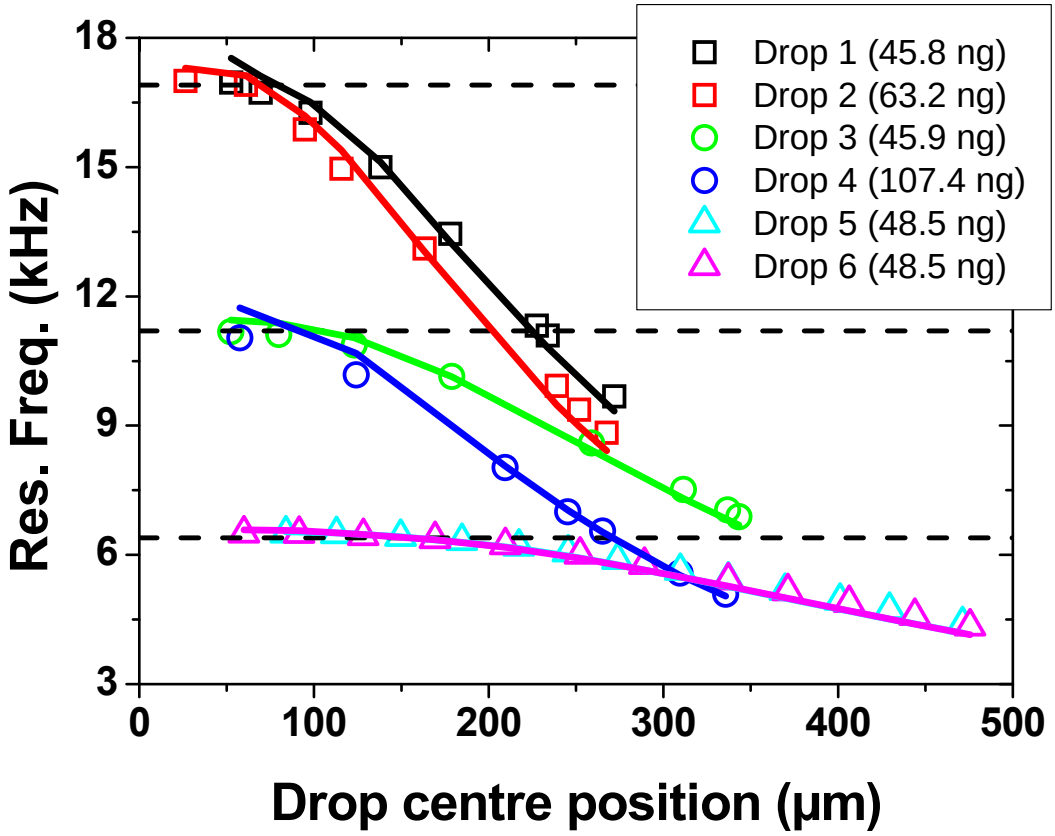

Figure 24. . Resonance frequency vs drop center position for three rectangular cantilevers. Cantilever properties: (D) l_0=297 μm, w=90 μm, d=1.05 μm, K_{TN}=0.178±0.01 N/m. (E) l_0=372 μm, w=90 μm, d=1.09 μm, K_{TN} =0.104±0.01 N/m. (F) l_0=503 μm, w=90 μm, d=1.18 μm, K_{TN} =0.053±0.005 N/m. Different drop masses used for each cantilever are shown on the figure. Experimental data points are represented by hollow symbols, simulations by solid lines. The horizontal dashed lines represent the three unloaded resonance frequencies as measured by the TN method.

The very good agreement between experiments and simulations makes the presented technique an interesting alternative to the added-mass method: the number of masses one can deposit is sufficiently large for any type of statistics (the error coming from the uncertainty in determining the exact position of the drops from the video images is counterbalanced by the large number of drops that can be deposited), and the reproducibility of the drop mass is very good (see masses of drops 5 and 6 in Fig. 24, e.g., noting that the two curves were acquired at different times). Moreover, the whole procedure is automated: after having determined the size of the drops, one can set the positions where we want to deposit them and we decide the number of cycles we want to run for

each cantilever. Then I start the data acquisition and record the resonance frequencies (curves like they are sketched in Fig. 24) and the contact radii. With these values, the automated inverse

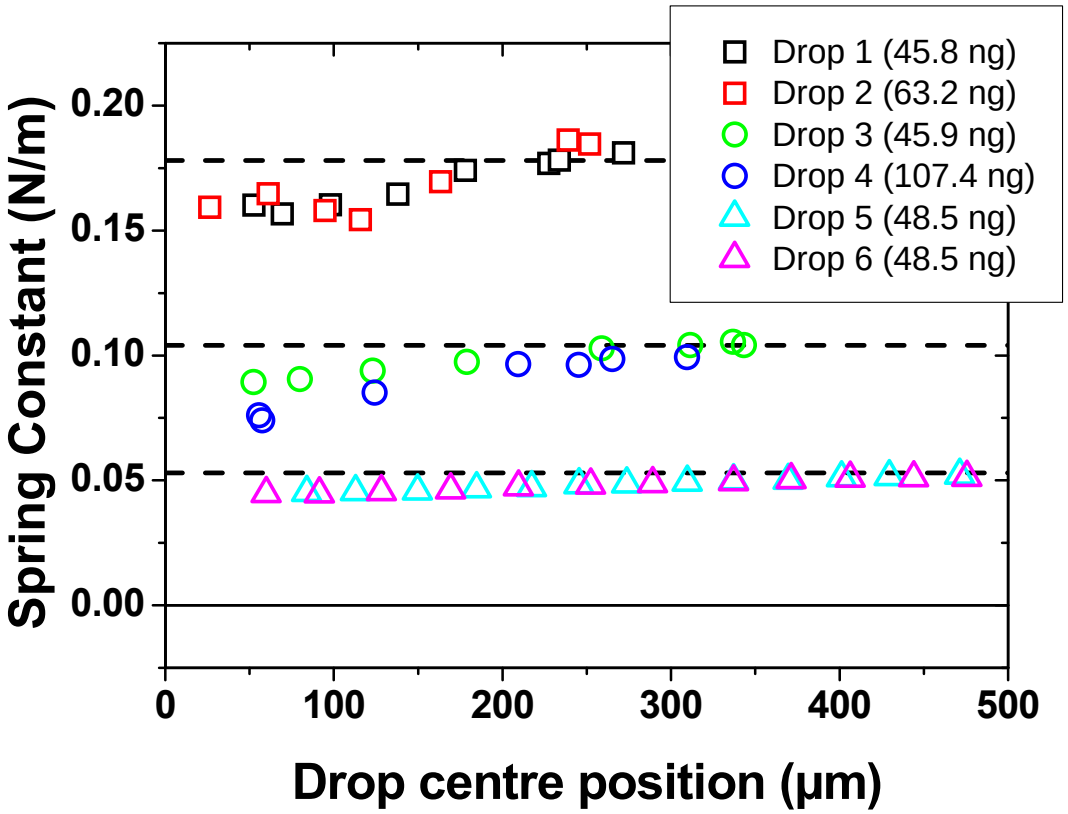

Figure 25. Spring constants of cantilevers (D), (E), and (F), plotted vs. drop center position. Spring constants determined by the TN method are plotted as horizontal dashed lines, while the mean value of the spring constants determined with the drop method are, respectively, K_{exp} =0.170±0.010 N/m, 0.098±0.006 N/m, and 0.048±0.002 N/m.

simulation cycle is started and we can identify the cantilevers' thickness for each of the 54 data points. Next, the mean thickness of each cantilever is calculated and inserted into Eq. (18). The results are the spring constants corresponding to each single data point, as shown in Figure 25. The results of the 54 simulated configurations differ for all data points by less than 6% from the experimental data, and only in one case the relative error is around 10%. This is also the expected error range of the calibration with the TN method. Inspection of the spring constant data presented in Figure 25 suggests that there is a systematic error, leading to a slope in the determined data points with the position of the drop center. I do not have an explanation for this yet; however, some facts can be excluded and one can speculate on some others. A parameter study with Poisson's ratio was performed and thus its influence can be excluded.

Cantilever type	l_0 (μm)	f_0 (Hz)	K_{TN} (N/m)	№ of drops	K_{exp} (N/m)	E_{rel} (%) $(K_{TN}-K_{experiment})/K_{TN}$
(A) Micromotive, rect.	**500**	**10404**	**0.19±0.01**	**7**	**0.198±0.012**	**4.2**
(B) Nanosensors, rect.	**460**	**11782**	**0.13±0.01**	**7**	**0.126±0.012**	**3.1**
(C) Veeco, triang.	**200**	**19253**	**0.10±0.01**	**3**	**0.096±0.002**	**4.0**
(D) Micromotive, rect.	**297**	**16900**	**0.178±0.01**	**2×8**	**0.170±0.010**	**4.5**
(E) Micromotive, rect.	**372**	**11215**	**0.104±0.01**	**2×7**	**0.098±0.006**	**5.8**
(F) Micromotive, rect.	**503**	**6400**	**0.053±0.01**	**2×12**	**0.048±0.002**	**9.4**

Table I. The six types of calibrated cantilevers, with spring constants measured according to the thermal noise (TN) and to the drop (experiment) method, and the relative error.

The magnitude of the simulated spring constant slightly changed, being largest for smallest Poisson's ratio, but the magnitude of the slope remained nearly unaffected. Therefore ν=0.26 was chosen, since it is a standard value from literature for crystalline silicon. One can also exclude the effect of the transversal bending of the cantilever caused by the drop [35], which is more pronounced when the drop is closer to the base of the cantilever, because this would cause a stiffening rather than a softening of the cantilever. More on the speculative side is that higher vibration modes are excited and become more pronounced when the drop is deposited closer to the base of the cantilever. This might be the reason of the systematic experimental error which leads to an "apparent" smaller spring constant. However, at the moment being it is not possible to confirm/ disprove this speculation using the simulation tools we are working with.

3.1.3 Conclusions

An extension to the existing added-mass method for the calibration of AFM cantilever spring constants is presented, and an automated simulation routine is developed. Instead of attaching particles of known masses to the end of cantilevers and measuring the resulting resonance frequency shift, the cantilevers are loaded with water microdrops with comparable masses. The microdrops were generated by a commercial inkjet dispenser, whose principal characteristic is to produce drops of extremely reproducible size. It is thus ideal for calibration tasks. Another significant advantage of water drops is that they allow for a nearly contactless calibration: no mechanical micromanipulation

of particles on cantilevers is required, neither for deposition nor for removal. After some seconds from generation, the water drop has completely evaporated, and no residues are left on the cantilever surface or tip. I applied two variants of the technique for calibrating the spring constants of six cantilevers: one by varying the drop size, and the other by varying the drop location. Both yielded results very close to the thermal noise calibration. The drop technique is practically suited for large cantilevers that are commonly used as micromechanical sensors. I have also shown, however, that with a little of experience smaller drops can be produced, enabling thus the calibration of cantilevers with dimensions around 200 μm, which are widely used in standard atomic force microscopy.

3.2 Evaporation of Microdrops from Atomic Force Microscope Cantilevers

3.2.1 Evaporation of Water and n-Alcohols from Hydrophobic Cantilevers

The method to trace evaporation of water microdrops from bare and silane modified atomic force microscope cantilevers by monitoring cantilever deflection was presented and discussed in detail in the work of Bonaccurso and Butt [34]. The authors pointed out that the evaporation process of a water drop can be traced with high sensitivity and time resolution. Another conclusion is that the evaporation is slowed down at the end due to drop thinning. The context of this chapter is to extend our knowledge on drop evaporation by using liquids with different vapor pressure to tune evaporation times and with different surface tensions to estimate the influence of substrate on evaporation process by monitoring vaporization of much less polar liquids from hydrophobic surfaces.

In my experiments I used drops of water and low molecular weight alcohols (see Table II). I deposited the drops in the middle of a cantilever hydrophobized by Perfluoro-1,3-dimethylcyclohexane (PPFC). The inclination data on the evaporation of a water drop deposited close to the base of a PPFC-coated cantilever are shown in Fig. 26A. The continuous line represents the experimental inclination of the cantilever and triangles represent the values calculated by Eq. (35) with $\boldsymbol{a}$ and Θ as obtained by video microscopy (see Fig. 26B). Calculated inclination values show the same tendency as the experimental signal, but are around 25 % lower than experimental values at t=0. The maximum deviation is when the drop reaches contact angle $\Theta=90^{o}$, after approximately 150 ms. During the evaporation, the contact angle continuously decreases, while the

contact radius is nearly constant within first 300 ms. The fact that the calculated inclination does not pass through the maximum at $\Theta=90^{o}$ as the experimental one does can not be explained. The data points calculated according to 2.5D model are significantly lower then experimental inclination.

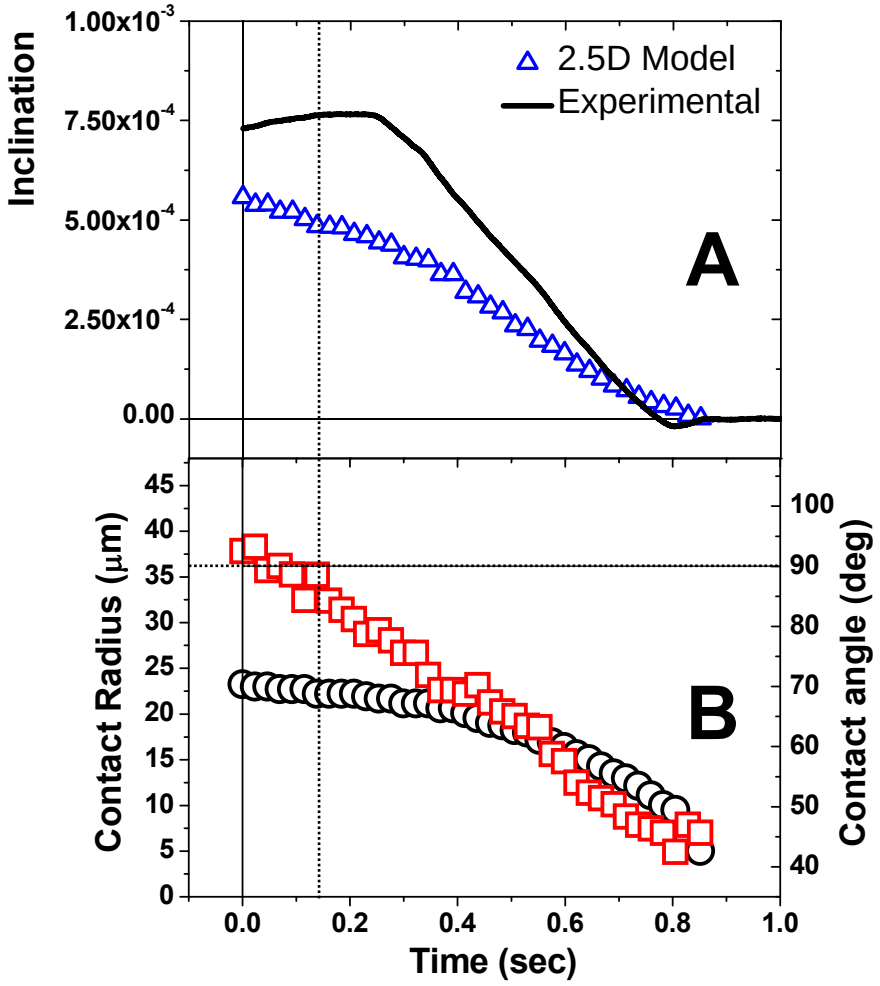

Figure 26. (A) Measured (continuous black line) and calculated (hollow blue triangles) inclination of the cantilever. Drop properties: mass=28.17 ng, initial contact angle and contact radius. Cantilever properties: l_0=750 μm, w=90 μm, d=1.288 μm, f_0=12 kHz, K=0.021 N/m. (B) Contact Angle (red squares) and contact radius (black circles). The dotted line indicates the time when $\Theta=90^{o}$. Thickness of PPFC=50.3 nm.

This can be due to, first, the specific interactions between the nonpolar hydrophobic surface of the cantilever and the polar OH-groups of water. Second, roughness of the PPFC surface plays a key role too leading to a contact angle different from the one for an ideally smooth surface. Both effects suggest a certain change in the surface stress of the cantilever underneath the drop [27, 57, 100, 101].

A series of similar experiments with drops of low molecular weight alcohols was carried out on the other cantilevers of the chip used for water drop deposition. So, the properties of the plasma deposited PPFC film remain practically the same. A drop of each following alcohol was deposited on a different cantilever of the chip. Differences in cantilevers' properties, as thickness and spring constant, are less then 1%. Properties of the used alcohols are summarized in Table II. The higher the molecular weight of an alcohol is, the lower is its vapor pressure, while its surface tension changes only slightly.

Liquids	γ, [N/m^2]	P_v, [Pa]
Methanol	**0.022**	**16900**
Ethanol	**0.022**	**7870**
1-Propanol	**0.023**	**2760**
1-Butanol	**0.025**	**860**
1-Pentanol	**0.026**	**259**
1-Hexanol	**0.026**	**110**
1-Octanol	**0.027**	**10**

Table II. Surface tension and vapor pressure of low molecular weight alcohols [100] used for drop evaporation experiments on PPFC-coated cantilevers.

Figure 27 represents contact angle and radius data on evaporation of a given series of alcohols. Figure 28 shows the correspondent cantilever inclinations. For a methanol drop on PPFC, constant contact angle mode (CCA) of evaporation is observed and no cantilever overbending was observed. In case of ethanol, no evaporation mode is observed, while for all the other alcohols the contact radius remains constant (CCR) at first followed by CCA mode, followed by a typical stick-slip (SS) behavior. This is found for many organic liquids on the PPFC-like surfaces [100].

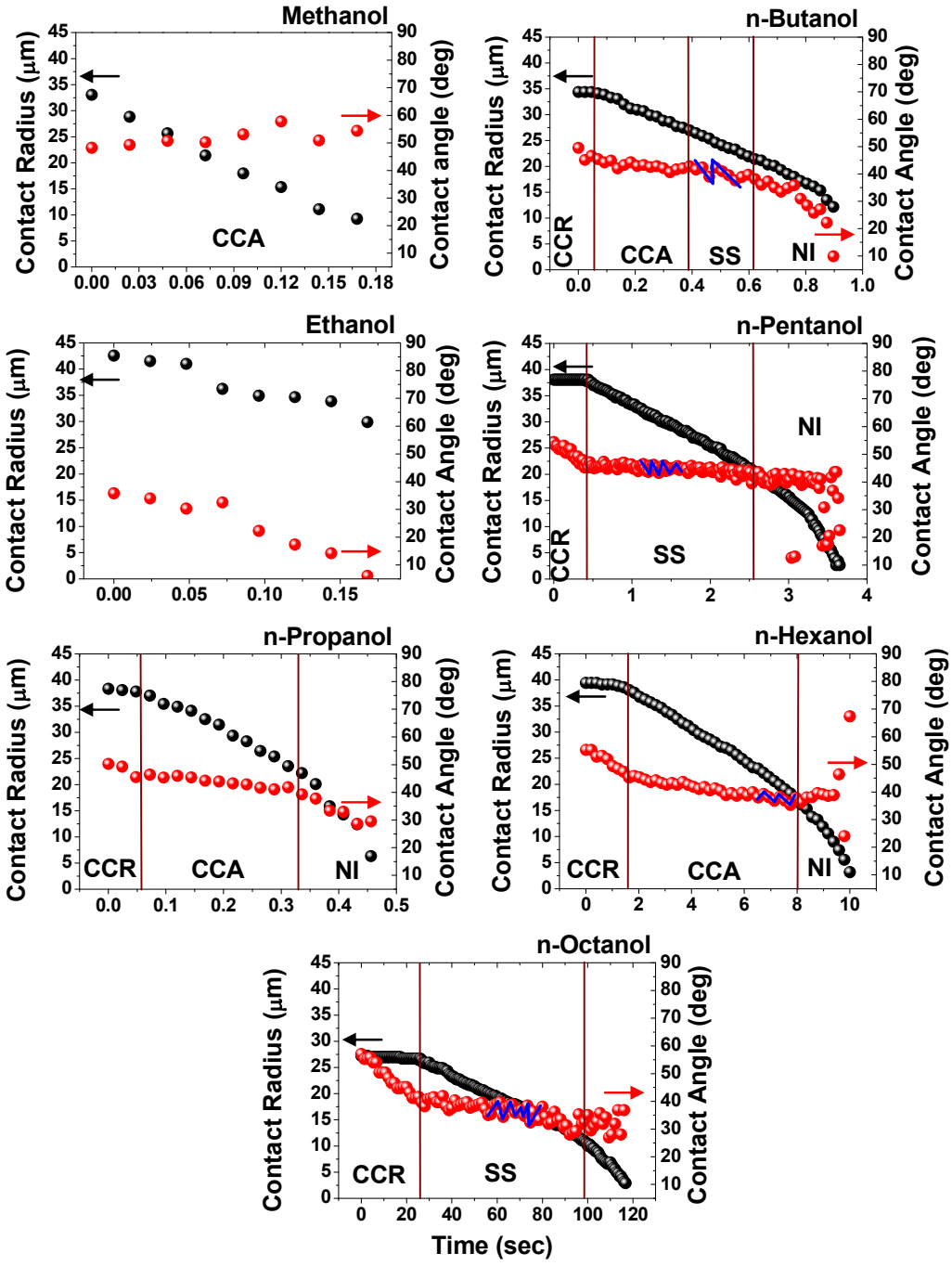

Figure 27. Evaporation modes of different alcohol drops on a hydrophobic cantilever surface. The cantilevers' properties deviate by less than 1 %. Thickness of PPFC d_{PPFC}=49±3 nm. Red dots are contact angle and black dots are contact radii. Blue zigzagged line highlights the Stick-Slip mode of evaporation (SS). NI – from this point Negative Inclination of the cantilever is observed.

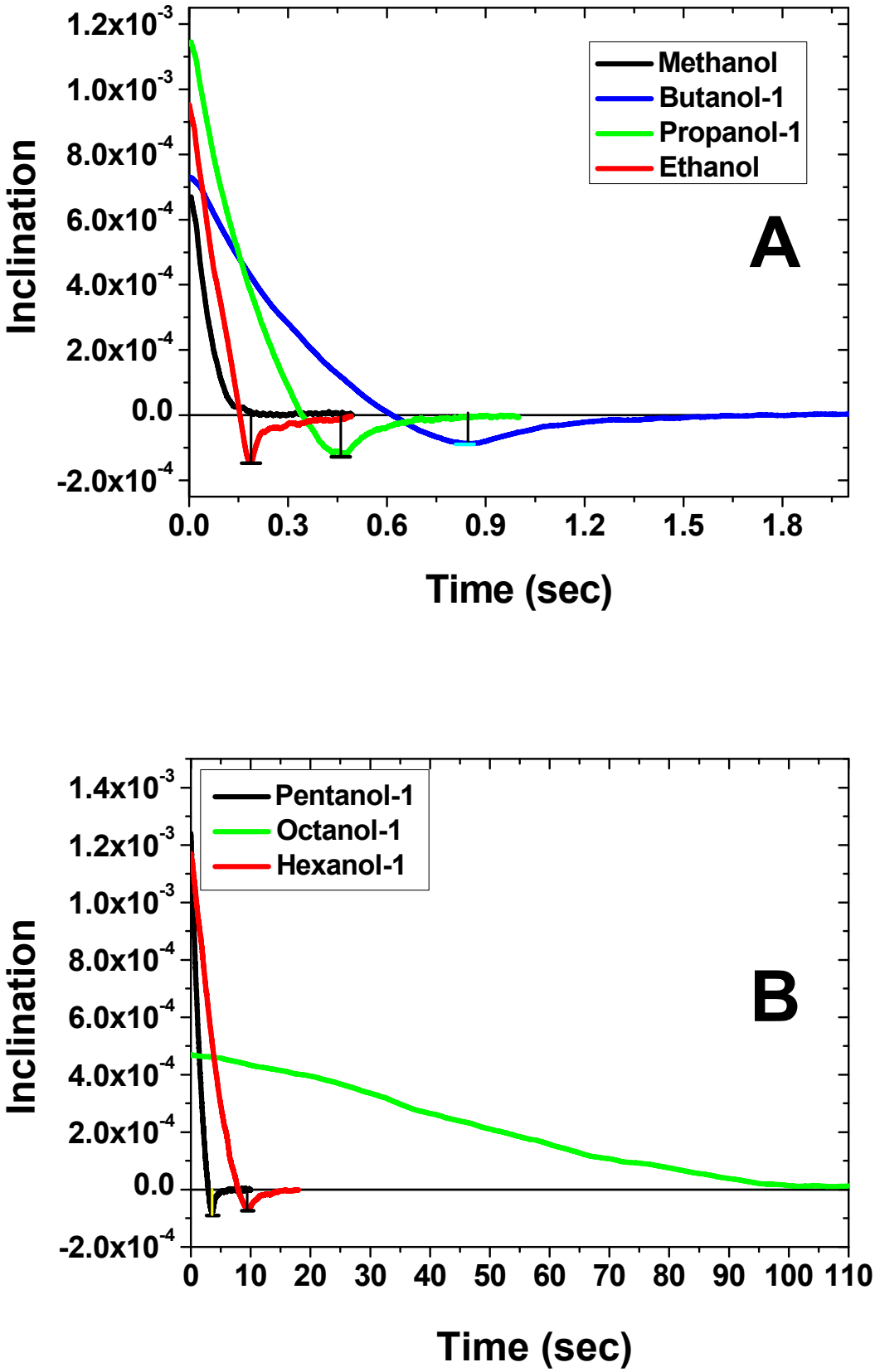

Figure 28. Cantilever inclinations measured for Methanol, Ethanol, 1-Propanol, 1-Butanol (A) and 1-Pentanol, 1-Hexanol, 1-Heptanol (B) drops.

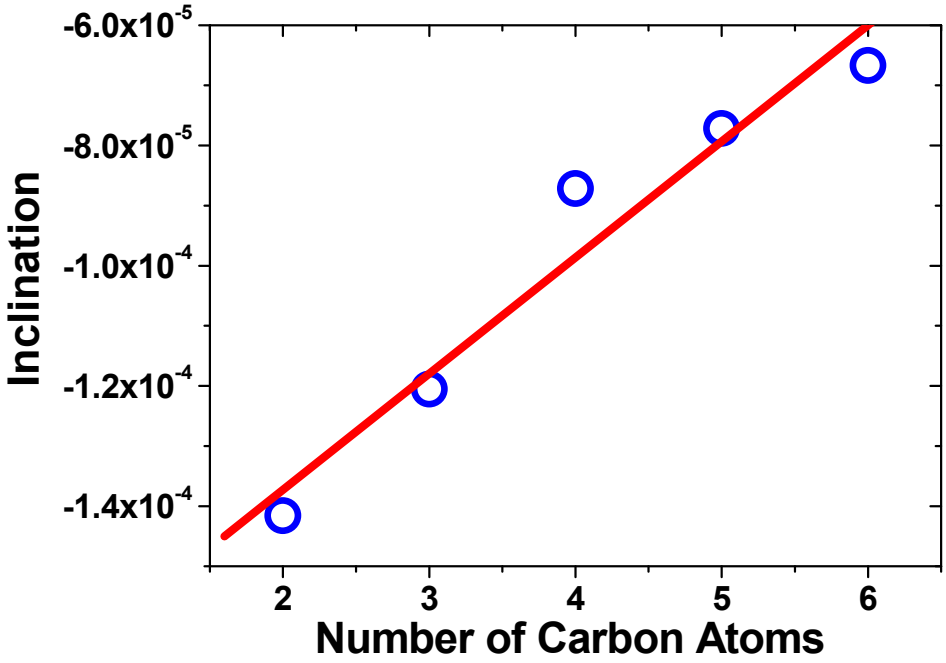

Figure 29. The "depth" of negative inclination with respect to the number of carbon atoms in alcohol.

The negative inclination is found for all alcohols, except methanol and n-octanol (Figs. 28A and 28B). Its numeric value is in linear correlation with the number of carbon atoms (Fig. 29), which cannot be explained so far. Equation 35 gives positive values accounting on surface tension effects acting at the drop rim, and, therefore, can not describe the negative cantilever inclination. This suggests that the degree of the polarity of the liquid together with its vapor pressure, are responsible for specific interactions at the liquid/solid interface. Correspondently the interfacial stress is changed, which leads to a cantilever overbending. We have no conclusive explanation yet why in case of n-octanol no negative inclination is found, neither in the case of methanol. Unfortunately, by measuring only the cantilever inclination during drop evaporation it is not possible to determine the mass remaining at the crossing with zero inclination. To solve this problem, in Chapter 3.2.3 a novel method to trace the cantilever inclination together with the drop mass is presented and discussed.

3.2.2 Cooling Effect due to Evaporating Water Drops

To monitor the cooling rate of an evaporating water drop on solid surfaces three types of experiments were carried out. First case, a drop of water is deposited on a bare silicon cantilever. The cantilever is bent only due to surface tension and stress effects [34]. This signal is compared with other two cases, when drops of water are deposited on cantilevers coated by a thin layer of gold

either on the upper side, or on the lower side. These bi-layered cantilevers are sensitive to thermal effects due to the difference in thermal linear expansion coefficients of silicon (α=2.6 μm/mK) and gold (α=17.6 μm/mK). When a drop is placed on the gold layer both, surface tension and evaporative cooling of the surface, make the cantilever bend upwards, i.e. towards the drop. When a drop is placed on the silicon side of the same cantilever, the surface forces are still pulling upwards, while the cooling makes the cantilever bend downwards, i.e. away from the drop.

By using the technique described in Chapter 2 it is only possible to measure the overall cantilever bending. To separate and quantify both effects FEM simulations are performed (see Chapter 2).

In Fig. 30 results on evaporation of the water drop from the bare silicon cantilever are shown.

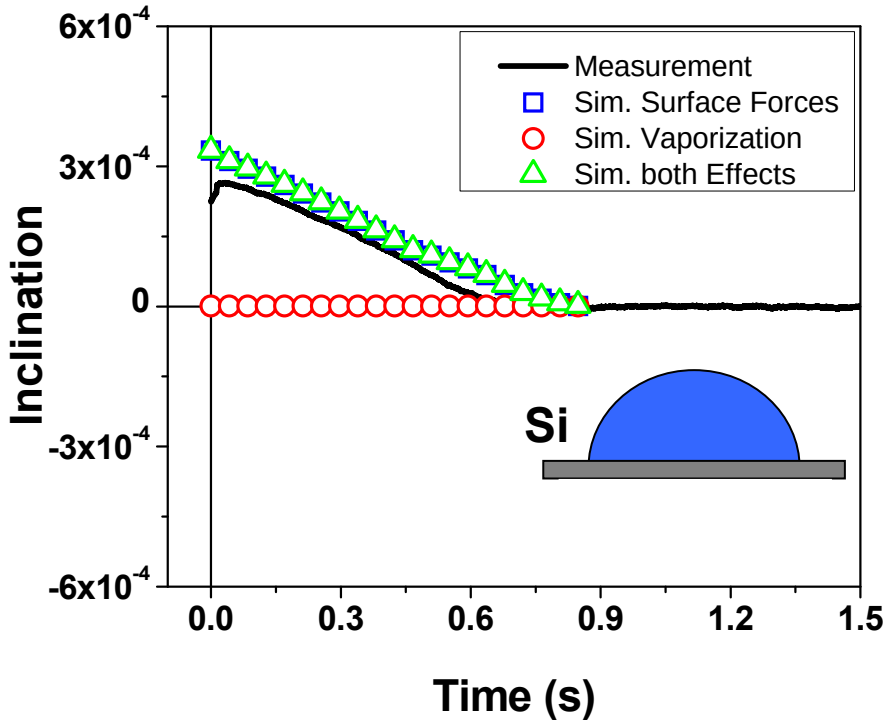

Figure 30. Experimentally measured (black curve) and simulated inclinations caused by surface tension effects (blue squares), vaporization (red circles) and combined effect (green triangles) on an uncoated bare silicon cantilever. Drop parameters: m=53.5 ng, initial radius a=42.32 μm, contact angle Θ=46.03°, l_{drop}= 43 μm – distance of the drop from the base. Cantilever properties: l_0=750 μm, w=90 μm, d=1.817 μm.

Only surface tension effects are expected to act. The continuous line represents the experimentally measured inclination, and colored symbols are used for the simulated inclinations. Blue squares show the cantilever inclination attributed to the surface tension as simulated with drop parameters changing in time and monitored by video. At the time of the drop, t=0, the measured inclination of

the cantilever has a maximum. Afterwards it progressively decreases until the evaporation is completed at t = 1. For the pure silicon cantilever no thermal effects are observed within the limits of this technique. Indeed, red circles represent simulated "zero" inclination (Fig. 30). The combined inclination is represented with green triangles. The difference between the simulated combined inclination and the measured one is around 10% at the beginning, and increases with time. That is mainly due to the error in determining contact angle and radius of the evaporating drop from the video microscopy, which also grows while the drop size decreases. Also not perfect crystallinity of the silicon can in part result in the not perfect matching between measurement and simulation. Residual mechanical stresses due to the microfabrication process of the cantilever may react to temperature changes and additionally bend the cantilever.

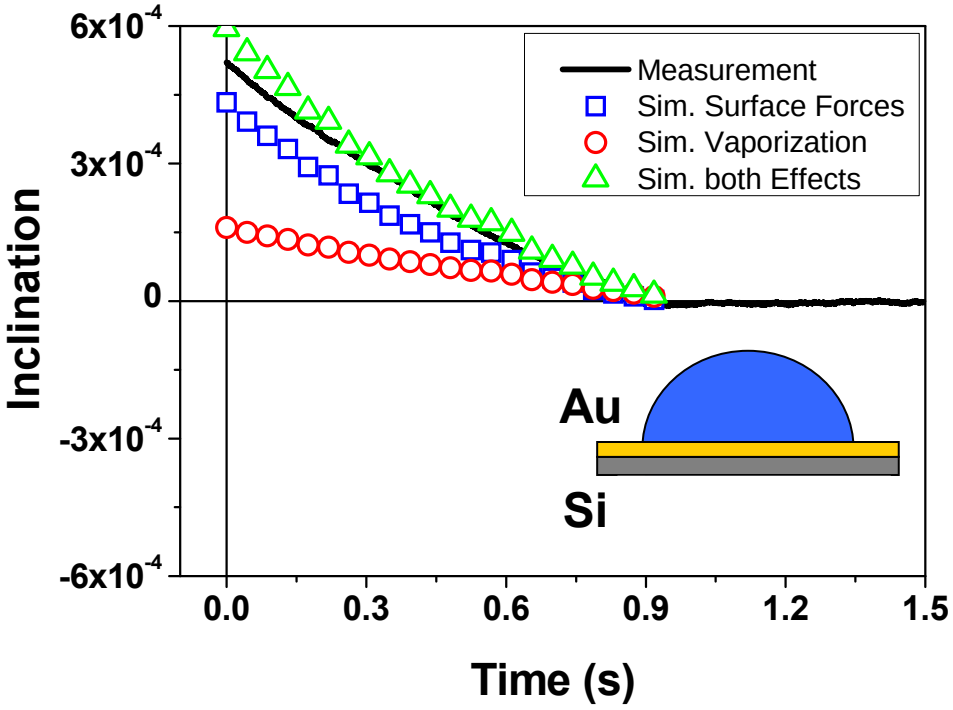

Figure 31. Experimentally measured (black curve) and simulated inclinations caused by surface tension effects (blue squares), vaporization (red circles) and resulting effect (green triangles) on silicon cantilever coated by gold on the top. Drop parameters: m=49.32 ng, initial radius a=32μm, contact angle Θ=76.85°, l_{drop}= 46 μm. Cantilever properties: l_0=750 μm, w=90 μm, d=1.466 μm.

If the top side of the cantilever, i.e. where the drop is deposited, is coated by gold, an overall resulting inclination which is larger than the one caused by surface forces alone is measured (Fig. 31). At t=0 the measured inclination curve has a positive value and remains positive until the

evaporation is completed at t=1. Both the curves of the simulated inclination due to surface forces only and to thermal effects are positive for all the evaporation time. Related to the heat flux, the inclination is maximum at the beginning, and gradually decreases to zero. The simulation on the combined effect of surface forces and thermal effects is not in such good quantitative agreement with the measured inclination as in the previous case. Especially at the beginning of the evaporation the difference is as high as 40%. Only towards the end of the evaporation, between t = 0.7 and t =1, the agreement is nearly ideal.

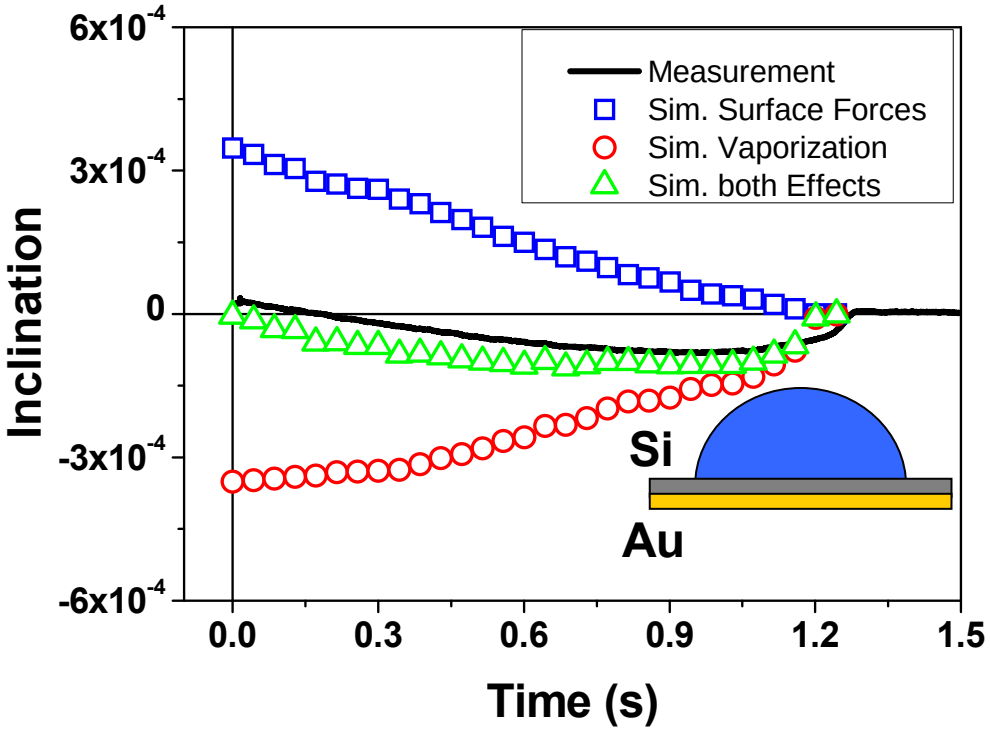

Figure 32. Experimentally measured (black curve) and simulated inclinations caused by surface tension effects (blue squares), vaporization (red circles) and resulting effect (green triangles) on silicon cantilever coated by gold from the back. Drop parameters: m=46.06 ng, initial radius a=41.26 μm, contact angle Θ=43.35°, l_{drop}= 108 μm. Cantilever properties: l_0=750 μm, w=90 μm, d=1.730 μm.

If the gold layer is at the bottom side of the cantilever, i.e. on the side opposite to that where the drop is deposited, we expect to measure an overall resulting inclination which is smaller than the one caused by surface forces alone (Fig. 32). In fact, the measured inclination curve has a positive value at t=0, it becomes negative at t ~ 0.1 and remains so until the evaporation is completed at t=1. The

curve of the simulated inclination due to surface forces only, according to drop and cantilever properties, is similar to the one of the previous experiment: the inclination is maximum at the beginning, and gradually decreases with time. The curve of the simulated inclination due to vaporization heat only, according to drop and cantilever properties, has negative values for all the evaporation time. The magnitude of the inclination is maximum at the beginning, and gradually decreases to zero. This is related to the heat flux, which decreases as the contact area of the evaporating drop becomes smaller. The combined effect of surface forces and thermal effects is in good quantitative agreement with the measured inclination curve, the average difference being below 10%. The not perfect matching between measurement and simulation is due to the issues already mentioned in the previous analysis.

The three water microdrops, despite of being of different initial volume and evaporating on two different surfaces, evaporate in a similar way as seen from the simulated inclination curves due to surface forces alone, which are directly related to the drop properties. The drop evaporating from the gold surface behaves only slightly different with respect to the drops evaporating from the silicon surface. This is indeed expected. On the other hand, the simulated inclination curves due to the vaporization of the drop are very different. The inclination is zero for the bare silicon cantilever, negative for the gold-on-bottom cantilever, and positive for the gold-on-top cantilever. The measured inclination curves, which are the result of the combined surface forces and thermal effects, differ also from each other, which is expected as well. These curves are extremely well reproduced by the FE simulations.

Herein, I showed that kinetics of drop evaporation and the resulting cooling of the surfaces can be successfully traced by bi-layered cantilevers. A FEM simulation model, used to separate and quantify surface tension and evaporative cooling effects, can be used to fit the experimental data.

3.2.3 A Method for Surface Stress Evaluation during Drop Evaporation

To be able to quantify the change in the surface stress at the solid/liquid boundary during drop evaporation I developed a new method which allows for tracing the cantilever inclination (surface tension and stress effects) and the resonance frequency shift (change of drop mass). The resonance frequency of a cantilever loaded by a drop can be monitored by amplification of its thermal oscillation. The method is tested on the evaporation of a water drop from a hydrophobic surface (HMDS) and on a bare silicon cantilever. In contrast to hydrophobized cantilevers, hydrophilic cantilevers bend negatively at the end of the evaporation. A model to describe the surface stress

involved in the negative inclination is suggested. In the end of this chapter, a comprehensive picture on the last stages of drop evaporation on hydrophilic surfaces is discussed.

3.2.3.1 Technique Validation

To validate the method, masses of the same evaporating drop acquired by means of video microscopy and from resonance frequency shift (Eq. (37)) are compared. For water drop evaporation, a hydrophobic (HMDS) surface is chosen since the most common mode of evaporation observed for such surfaces is constant contact angle. As a consequence, pinning of a drop can be avoided and water-surface interactions are weak. Figure 33 shows two mass curves of the same water drop in time. The initial drop mass is 61.03 ng. Reversed blue triangles are data points for drop mass found from the frequency shift and red hexagons represent the mass of the drop found from

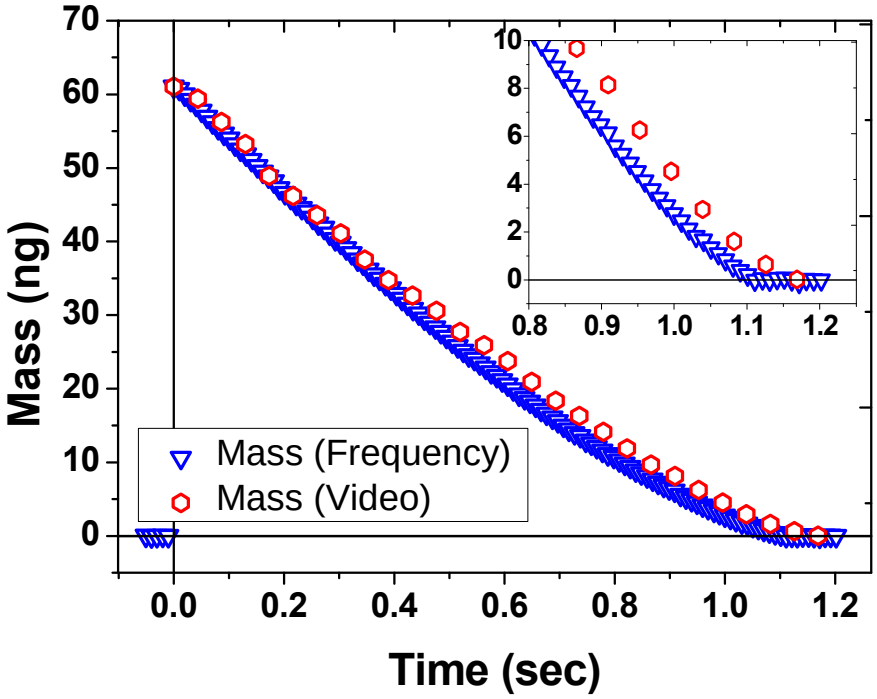

Figure 33. Comparison of two techniques: mass loss during drop evaporation from hydrophobic HMDS surface determined from video (red hexagonals) data and frequency shift (blue inversed triangles). Initial mass of evaporating drop is 61.03 ng and determined from drop parameters taken by video in the beginning. This mass is attributed to correspondent resonance frequency measured at the same moment. The inset shows zoom at the end of evaporation.

video data. Both curves overlap nearly perfectly. For the mass, calculated from the resonance frequency of the cantilever, the time resolution (~ 5 ms) and the sensitivity (~ 50 pg) is much higher than those for the video microscopy. This allows for studying drop evaporation closer to its end; see Fig. 33 (inset). The evaporation process slows down at its end. This is observed from video data. The inset of Figure 33 shows this in more details. Starting from t=0.6 the slope of the data points changes. The fact that the evaporation of water drops slows down, first, is expected from the linear change of $V^{2/3}$ in time [46] that predicts slowing down, and, second, can take place due to several reasons and is completely not yet understood. One of the reasons could be contamination on the surface that interacts stronger with liquid thus slowing down its evaporation. It is important to note that the proposed technique allows for much higher time resolution for mass sensing. Thus extremely small amounts of liquid can be traced which cannot be done by the video microscopy.

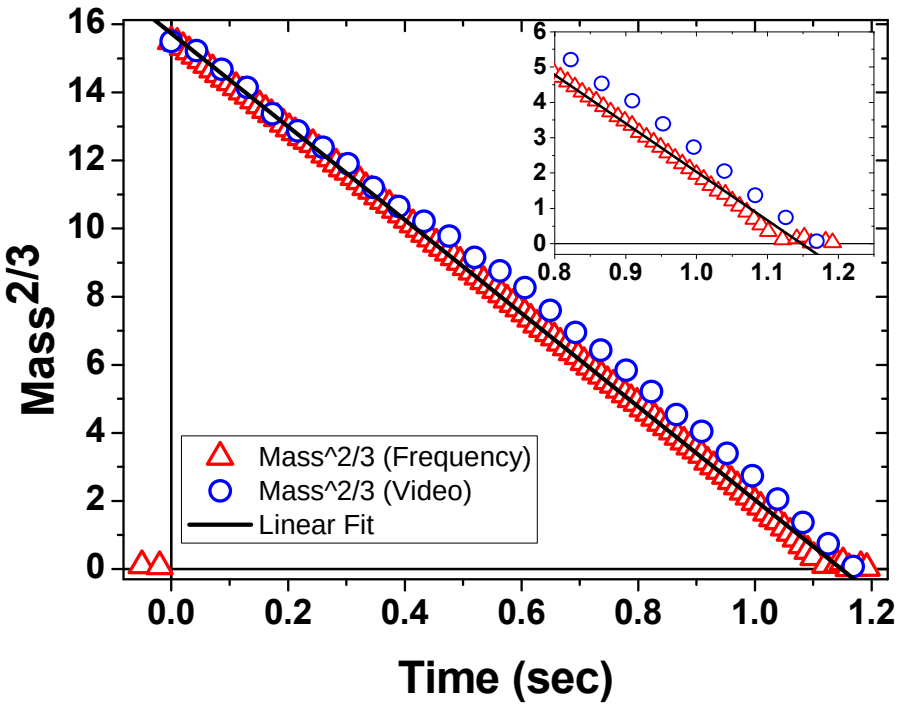

Figure 34. Linear plot of the same drop mass $m^{2/3}$ vs. time according to the change in volume $V^{2/3}$ in ambient atmospheric conditions (see Eq. 21) when evaporation is mainly driven by diffusion.

To confirm that the drop of water evaporates in accordance with Eq. (15) in ambient atmosphere, when the evaporation process is mainly driven by diffusion of a liquid vapor, the mass data to the power of 2/3 is plotted versus time (Fig. 34) for two types of measurements. A line can be fitted in

case of the mass calculated from the frequency shift. The mass from video data deviates slightly from this line. This deviation is negligible, and can be explained by the instrumental error while acquiring and extracting drop parameters from the video data.

From the cantilever inclination and the drop mass I can calculate the contact radius ***a*** and the contact angle Θ by solving the system of following equations

$$\begin{cases} \dfrac{dz}{dx} \approx \dfrac{3\pi a^3}{Ewd^3}\gamma \sin\Theta & (39) \\ m = \dfrac{1}{6}\pi\rho h\left(3a^2 + h^2\right) & (40) \\ \Theta = 2arctg\left(\dfrac{h}{a}\right) & (41) \end{cases}$$

The mass of the drop ***m*** can be found using Eq. (37) and ***h*** is the height of the drop. The simultaneously acquired inclination and mass from one experimental measurement for the same drop with its initial mass of 61.03 ng are shown in Figure 35. The red stars represent the mass during evaporation, the blue hollow circles the cantilever inclination. Similar curves are representative for most measurements been made with water drops on clean, hydrophobized silicon cantilevers. The cantilever inclination reaches its maximum when a half of initial drop mass is evaporated at around 450 ms. This agrees well with Eq. (35) suggesting that contact angle approaches 90°. Indeed, solving Eqs. (39-41) one obtains contact angle and radius calculated from drop mass and cantilever inclination data. The results of such calculations are shown in Figure 36, where contact angle and radius obtained by video microscopy and from frequency shift. In the beginning of evaporation process the drop evaporates according to the constant contact radius mode (CCR). When the contact angle decreases to 90° at ***t***=450 ms, the maximum cantilever inclination is attained. Afterwards, the evaporation mode changes to constant contact angle mode (CCA), followed by a mixed mode (SS). Both experimental methods yield very similar results, though ***a*** and Θ obtained from resonance frequency have a better time resolution. Using cantilevers as highly sensitive sensors for the surface forces and the mass of the drop the evaporation can be followed by monitoring independently the inclination and the resonance frequency of the cantilever. We can record the inclination curve with a temporal resolution of ~ 0.1 ms between data points, and the frequency curve with ~ 5 ms (the mass sensitivity ~ 50 pg). The evaporation law "$\boldsymbol{V^{2/3}}$ ***vs. time***" (Eq. (15)) is extended to microscopic drops. From the cantilever inclination and the drop mass contact angle Θ and radius ***a*** of the drop can be calculated until nearly the end of the evaporation. This method is applicable for a case of

hydrophobic surfaces and allows to measure more drop parameters simultaneously for smaller drop sizes.

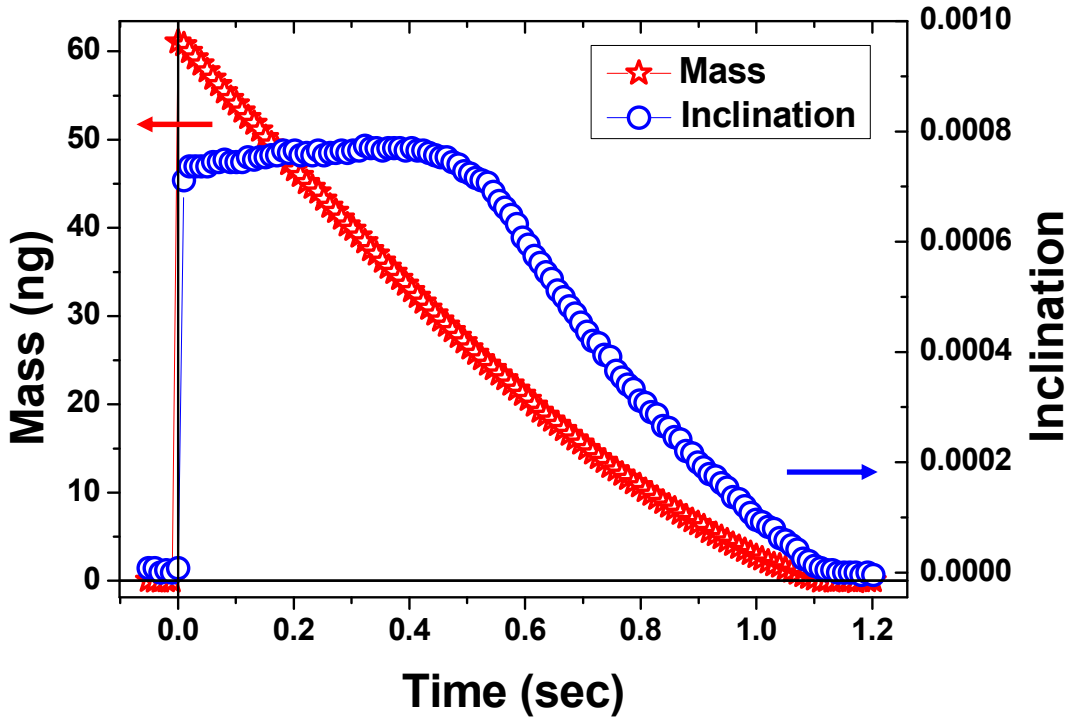

Figure 35. Two simultaneous measurements of: drop mass (red stars) and cantilever inclination (blue circles) for a water drop on a HMDS hydrophobic surface. Initial drop mass=61.03 ng. Cantilever properties: l_0=705 μm, w=90 μm, d=0.865 μm, K=0.0074 N/m, f_0=2379 Hz and the frequency measured when the drop hits the cantilever surface f_{drop}=1815.61 Hz.

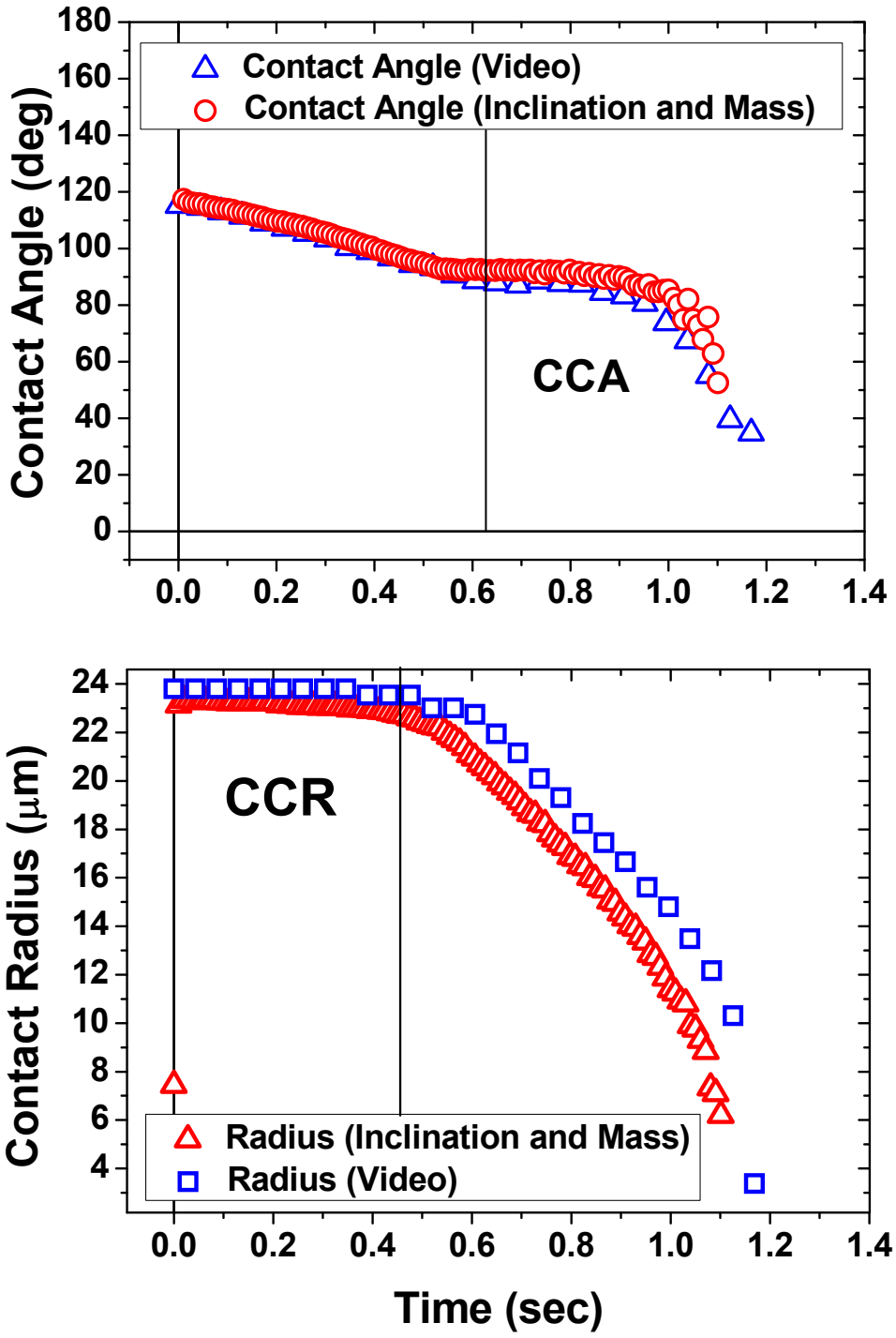

Figure 36. Comparison of contact angle and contact radius data measured by video (blue triangles and squares) and found as solutions (red circles and triangles) of the system equations (Eq.). CCA – constant contact angle and CCR – constant contact radius modes of evaporation.

3.2.3.2 Negative Inclination and Surface Stress Evaluation

In contrast to the previous case, when a drop of water was deposited on a clean and smooth hydrophobic cantilever surface and the cantilever inclination was only positive, the evaporation of water drops from bare clean silicon cantilevers looks different (Fig. 37). A negative inclination at the end of the evaporation is observed. Red stars show the mass change and blue hollow circles show the cantilever inclination in time. The drop parameters acquired by video images are

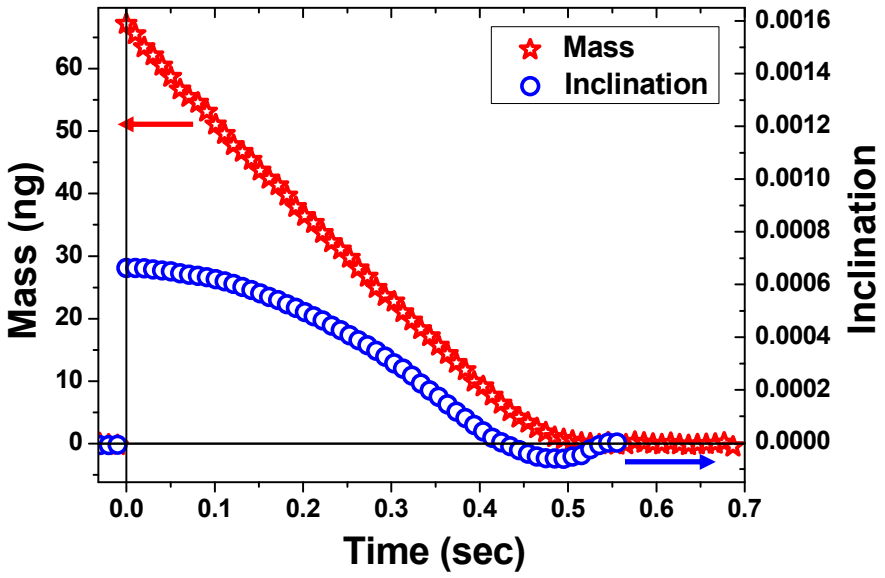

Figure 37. Two simultaneous measurements of: drop mass (red stars) and cantilever inclination (blue circles) for a water drop on a bare silicon cantilever. Initial drop mass=67.15 ng. Cantilever properties: l_0=743 μm, w=90 μm, d=1.238 μm, K=0.0187 N/m, f_0=2892.65 Hz and the frequency measured when the drop hits the cantilever surface f_{drop}=2543 Hz.

shown in Fig. 38A. The drop evaporates mostly according to the CCR mode, typical for water drops on hydrophilic surfaces. Only at t=500 ms the radius starts to decrease. At around t=400 ms the cantilever inclination crosses the time axis and becomes negative.

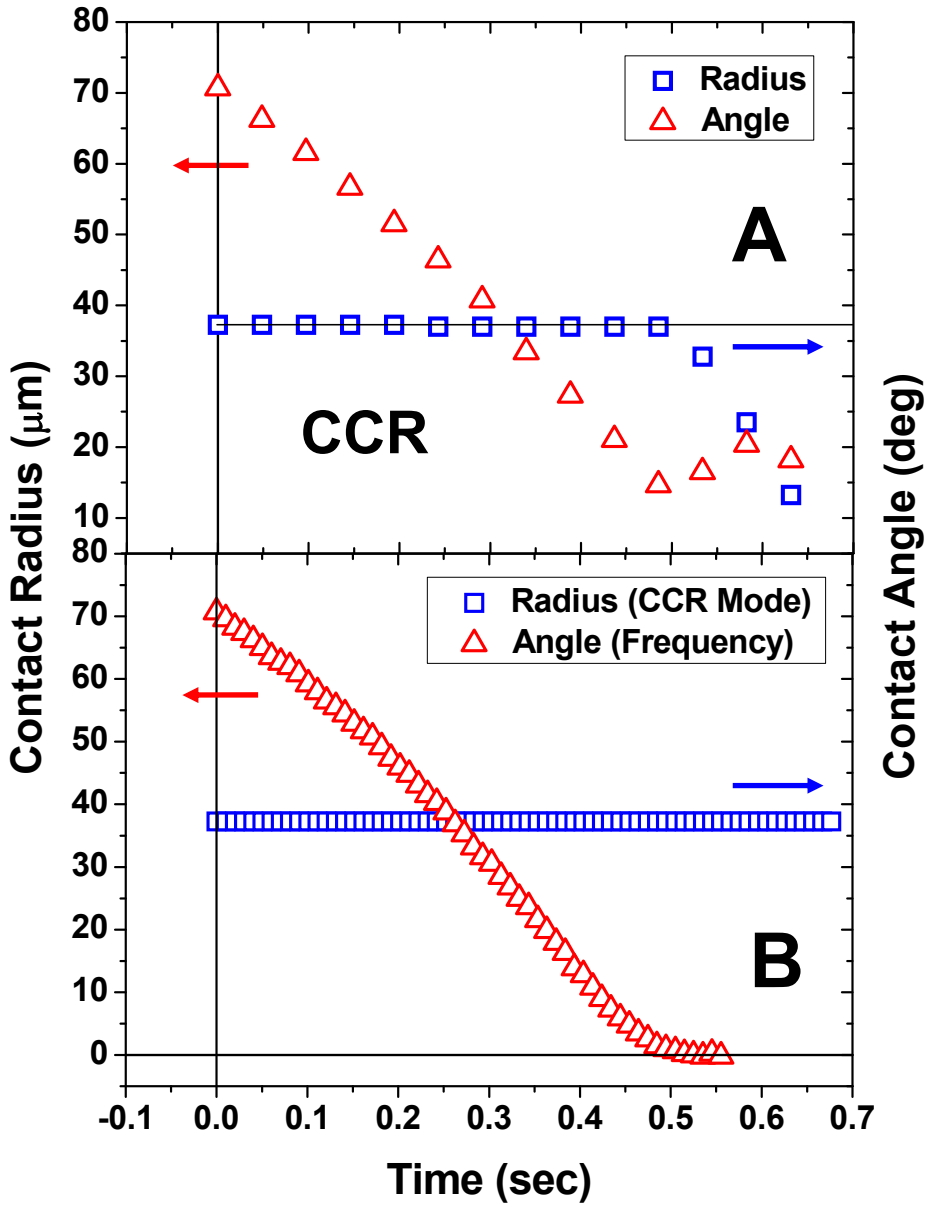

Figure 38. Experimental values of contact angle (red triangles) and radius (blue squares) for a drop of water evaporating from the bare silicon cantilever (A). Contact radius set constant and Contact angle calculated using Eqs. (40) and (41) (B).

The negative inclination can not be described in terms of the model given by Eq. (35) since it contains only positive terms. One free parameter representing the additional change in surface stress ΔS has to be added to Eq. (34):

$$\frac{dz}{dx} = \frac{\pi a^3}{4EI}\left[\gamma \sin\Theta + \frac{2d}{a}\left(\gamma\cos\Theta - \gamma_S + \gamma_{SL}\right)\right] + \Delta S \qquad (42)$$

ΔS must be negative and not constant over the evaporation process. The origin of negative bending can be explained with the following picture (Fig. 39).

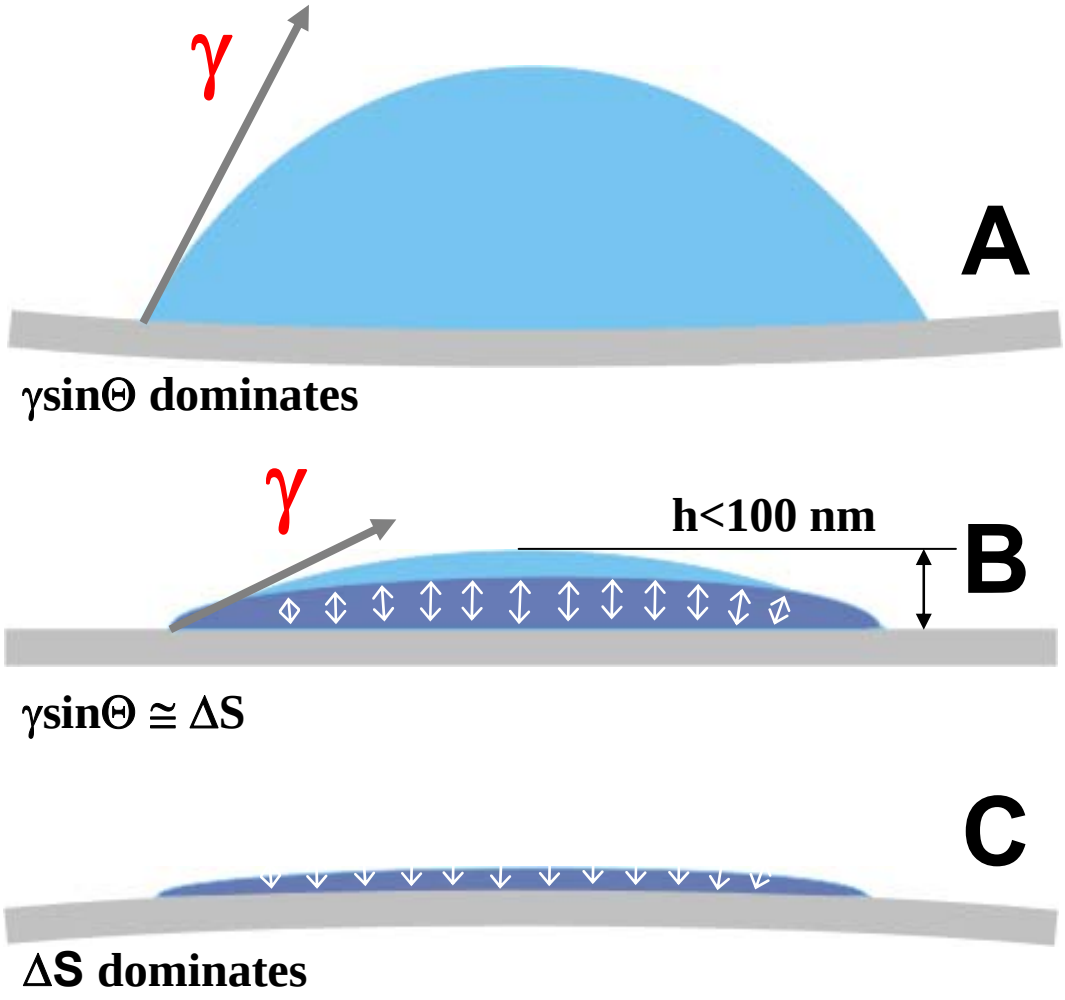

Figure 39. Tentative interpretation for the negative inclination of the cantilever arising at the last stages of drop evaporation. (A) surface tension (gray arrow) effects dominate for relatively big contact angles in the beginning and in the middle of the evaporation, (B) when contact angle decreases enough van der Waals forces (small white arrows) acting between two approaching liquid/air and liquid/solid interfaces enforce begun flattening of the drop, thus converting it into a thin film (C).

When the contact angle is relatively big, the drop pulls the cantilever upwards. The first term of the Equation (42) dominates over the second term which is zero under assumption of Young‘s Equation (1), and the surface stress term is also set to zero. From the measurements it is known (see also Fig. 38A), that drops evaporating on hydrophilic surfaces do this mainly in the CCR mode, i.e. the rim is

pinned over the entire process. Thus the contact angle is continuously decreasing. When the drop becomes thinner than some 100 nm, attractive van der Waals (vdW) forces begin to act between the upper and the lower drop surface, causing an even faster flattening of the drop (see Fig. 39B). Laplace pressure, surface tension, and vdW forces have a similar magnitude. When the surface stress term dominates, the remainings of the drop wet the surface and form a thin film (see Fig. 39C), which probably spans a larger area than the original drop contact area. Since the interfacial tension between film and cantilever is smaller than between air and cantilever, the cantilever bends away from the drop, and the measured signal is negative.

For a quantitative evaluation of ΔS, I applied the following procedure. From video microscope images it is known that the drop evaporates in CCR mode (see Fig. 38A) as far as the resolution of the technique allows to judge. I assumed that the CCR mode holds until the end (last 100 ms). From the measured mass, and knowing the contact radius (see Fig. 38B), I calculate the magnitude of the inclination curve as if only the vertical surface tension and the Laplace pressure were acting on the cantilever. Subtracting these two curves I obtain the curve of the unknown stress. This is illustrated in Fig. 40. Reversed black triangles represent the initial experimental curve. Blue hexagons show the calculated inclination accounting only on surface tension effects. The red stars are calculated surface stress.

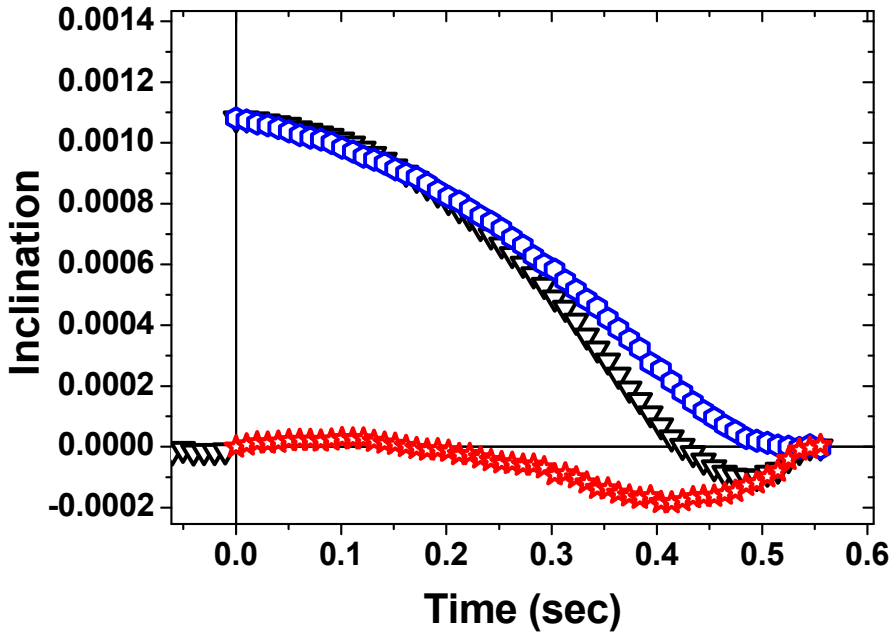

Figure 40. From the data presented in Fig. 38B a positive "non-zero inclination" (blue hexagonals) is calculated. By subtracting calculated inclination from experimental inclination (inversed black triangles) a surface stress related part of overall inclination can be found.

Using cantilevers as sensitive stress sensors an effect arising at the end of the evaporation of pinned microscopic drops was found to take place on hydrophilic surfaces. So far, this effect was never observed by means of other methods. By monitoring the inclination of the cantilever and the drop mass, and accounting on the evaporation mode (CCR) this effect can be quantitatively evaluated. At the end of the evaporation a drop converts into a thin liquid film which wets the surface, reduces the surface tension under the film, and causes the cantilever to bend away from the film.

3.2.4 Evaporation of Drops in Saturated Atmosphere

3.2.4.1 Experiment

To verify the theoretical results on considerations of nonequilibrium effects during the evaporation of small drops (see Chapter 1) a set of experiments in quasi-saturated water vapor atmosphere was carried out. Water drops of different sizes were deposited as described in Chapter 2. A reproducible contact angle of 90 ± 5^{o} was obtained for all drops at the beginning of evaporation. It further remained constant for at least half the evaporation time. The first part of the evaporation process followed the predicted evaporation law (Eq. (15)) and $V^{2/3}$ decreased linearly with time (Fig. 41). When extrapolating this linear part to full evaporation, typical evaporation times ranged from 70 to 350 s. To a large part this variation is caused by the different initial volumes, and compared with time constants calculated using Eq. (14) in Fig. 42. For example drop 1 in Figure 41 evaporated within 5 min, starting with an initial volume of 107.000 μm^3. During the first 100 s it followed the evaporation law. If a diffusion coefficient of $D = 2.4\times10^{-5}$ m^2/s for water in air at room temperature is assumed, a contact angle of 90° is used ($f = 0.53$, $\beta = 2$) and the experimental slope of the graph $V_L^{2/3}$-versus-time is taken, I find with Eq. (14) a value for the humidity of 99.1% ($x = 0.009$). This agrees with the measured value of 99%. The same result is obtained if one uses the evaporation of drop 2 for the first 60 s. The fact that the atmosphere seems to be not perfectly saturated is probably caused by tiny holes of the sealing of the Parafilm, or in small temperature differences across the vessel. For drop 3 a slightly lower humidity of 98.7% is calculated. In this case the nozzle of the dropper was shifted during the experiment and this caused a leak in the seal of the Parafilm around the nozzle. In some cases, for example for drop 3, after an initial fast phase the evaporation process slowed down significantly and a slower phase of evaporation was observed (inset Fig. 41). This led to long evaporation times of over 350 s, which can not be explained by the fact that the contact angle changed during evaporation.

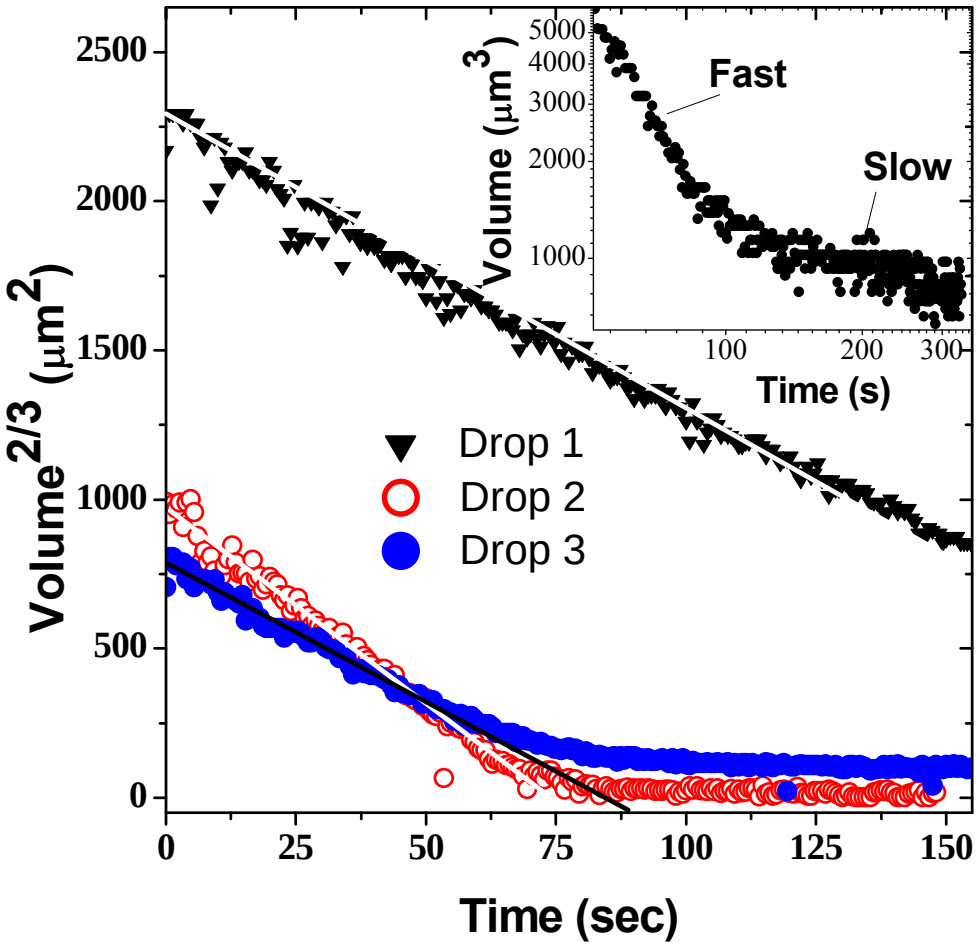

Figure 41. Change of volume of three water drops $V_L^{2/3}$ evaporating from hydrophobized silicon cantilevers at high RH. The straight lines are linear extrapolations. Inset: V_L-versus-time on a double logarithmic scale.

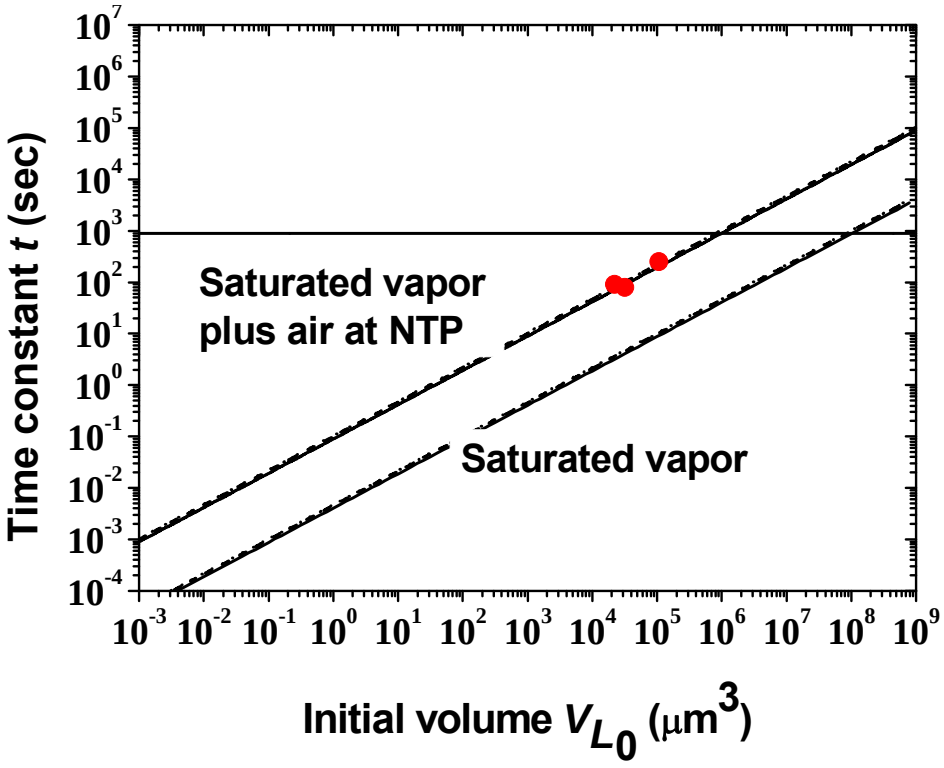

Figure 42. Time of evaporation (•) of a sessile water drop at 25°C versus the initial volume as calculated for 99% humidity with Eq. (14).

3.2.4.2 Conclusions

To conclude, in an open system, a drop of a volatile liquid sitting on a hard, flat surface is never in thermodynamic equilibrium. Eventually it will evaporate. Since the curved liquid surfaces possess an increased vapor pressure as compared to flat surfaces, the drop will eventually evaporate, as quantified by Kelvin's equation. As a consequence, it is not possible to derive Young's equation on thermodynamic grounds for open systems. However it does not mean that Young's equation is not valid for this case. Young's equation can not be derived thermodynamically. Moreover, the contact angle is not a thermodynamic quantity for a sessile drop due to its constant change during evaporation the influence of which is significant for small drops. Only in a small, closed system a drop can be in thermodynamic equilibrium in its vapor atmosphere. For practical reasons it is useful to compare the time of evaporation with the duration of the measurement of a contact angle. If the time of the experiments is much shorter than the evaporation time, evaporation can be neglected and Young's equation can be used safely. That is not the case for microdrops which evaporate fast. Thus for microdrops Young's equation is of reduced significance. A critical drop volume can be defined for a given observation time. Only drops with a volume much larger than this critical volume show negligible evaporation. For drops smaller than this critical volume, evaporation effects are significant.

Summary and Conclusions

A cantilever based method to trace the evaporation dynamics of drops was developed. With this technique was found that on both, hydrophobic and hydrophilic surfaces, the evaporation of water drops significantly slows down at its end. This effect is more pronounced for the hydrophilic surfaces. On hydrophobic surfaces a single measurement with a silicon cantilever provides data for the drop mass, contact angle and radius until very close to complete evaporation. On hydrophilic surfaces, it is as well possible to measure drop mass and inclination of the cantilever. In this type of the experiments the cantilever inclination is negative at the end of the evaporation process. Negative inclination mostly occurs when drops are pinned. This effect can not be detected with any of the other well-established methods. A model to evaluate surface effects during drop evaporation and specifically at its end is provided. According to this, close to the evaporation end a thin liquid film wets the surface, reduces the surface tension on the upper side, and the cantilever bends down. This surface effect has been directly measured only with this method up to now.

Atomic force microscope cantilevers coated by gold on one of their sides were successfully used as heat sensors for the evaporative cooling measurements of microdrops. Water drops with diameters smaller then 100 μm were deposited on three different types of cantilevers: pure silicon cantilevers, silicon cantilevers with a gold coating on the top, and silicon cantilevers with a gold coating on the bottom side. Using the optical lever technique the resulting bending of the cantilevers was measured. With the help of FEM simulations the effects of surface tension and evaporative cooling were separated and quantified for an evaporating microdrop. The experimental results were reproduced with high accuracy. Differences between the experiments and the simulations are in large part due to the limitations of the video technique used to measure the dimensions of the evaporating drops: the error increases with decreasing drop size. Moreover, the material properties of the cantilever are not ideal: mechanical stresses are a residual of the microfabrication process of the cantilevers. Unfortunately, they affect the mechanical response of the cantilevers to external stimuli, and they can not be quantified a priori. The FE simulations also allow to calculate the temperature distribution

inside the cantilever, and thus to quantitatively evaluate the cooling originating from an evaporating drop.

The applicability of Young's equation was verified for microdrops. It was shown that Young's equation can not be applied to microscopic drops due to their fast evaporation. A study on evaporation of microdrops in saturated vapor atmosphere was performed to estimate evaporation times and compare them with a theory developed, which relates the initial drop volume with the overall evaporation time. Drops were deposited on a hydrophobic surface at 99% relative humidity. The constant contact angle mode of the evaporation was observed during all the evaporation process. The evaporation times for water microdrops agreed well with the theoretically estimated ones and varied within 75÷300 seconds. This is much smaller than 15 minutes being the criterion for the critical volume of a drop evaporating within this time. Thus for water drops with diameters smaller than 100 μm Young's equation is of significantly reduced applicability due to evaporation effects.

In conclusion, in this work I investigated the evaporation dynamics of water microdrops deposited on atomic force microscope cantilevers, which were employed as sensitive stress, mass and temperature sensors with high time resolution. The technique has some advantages with respect to video-microscope imaging and ultra-precision weighting with electronic microbalances or quartz crystal microbalances, since it allows to measure more drop parameters simultaneously for smaller drop sizes. The technique further allows to detect differences between water microdrops evaporating from clean hydrophilic and hydrophobic surfaces. The difference is especially manifest close to the end of evaporation. The evidence arises that on the hydrophilic surface a thin water film forms, while this is not the case for the hydrophobic surface. Metal coated cantilevers can be used as thermometers, and allow to precisely measure the temperature of an evaporating microdrop. This can be relevant for further applications of cantilevers as calorimetric sensors for chemical reactions taking place in drops on their surface.

References

1. Shedd, T.A., *Next generation spray cooling: High heat flux management in compact spaces.* Heat Transfer Engineering, 2007. **28**(2): p. 87-92.
2. Shedd, T.A. and A.G. Pautsch, *Spray impingement cooling with single- and multiple-nozzle arrays. Part II: Visualization and empirical models.* International Journal of Heat and Mass Transfer, 2005. **48**(15): p. 3176-3184.
3. Fabbri, M., S.J. Jiang, and V.K. Dhir, *A comparative study of cooling of high power density electronics using sprays and microjets.* Journal of Heat Transfer-Transactions of the Asme, 2005. **127**(1): p. 38-48.
4. Chou, F.C., et al., *Cooling of microspot by microdroplets.* Japanese Journal of Applied Physics Part 1-Regular Papers Short Notes & Review Papers, 2004. **43**(8A): p. 5609-5613.
5. Socol, Y., et al., *Method for in situ measurements of ink jet printed ink drops.* Journal of Imaging Science and Technology, 2004. **48**(1): p. 15-21.
6. Sirringhaus, H., et al., *High-resolution inkjet printing of all-polymer transistor circuits.* Science, 2000. **290**(5499): p. 2123-2126.
7. Heilmann, J. and U. Lindqvist, *Effect of drop size on the print quality in continuous ink jet printing.* Journal of Imaging Science and Technology, 2000. **44**(6): p. 491-494.
8. Bonaccurso, E., et al., *Fabrication of microvessels and microlenses from polymers by solvent droplets.* Applied Physics Letters, 2005. **86**(12).
9. Tullo, A.H., *Gradual evolution.* Chemical & Engineering News, 2002. **80**(42): p. 32-+.
10. Deegan, R.D., *Pattern formation in drying drops.* Physical Review E, 2000. **61**(1): p. 475-485.
11. Deegan, R.D., et al., *Contact line deposits in an evaporating drop.* Physical Review E, 2000. **62**(1): p. 756-765.
12. He, J., et al., *Drying droplets: A window into the behavior of nanorods at interfaces.* Small, 2007. **3**(7): p. 1214-1217.

13. Leng, J., et al., *Microevaporators for kinetic exploration of phase diagrams.* Physical Review Letters, 2006. **96**(8).
14. Zimmermann, M., et al., *Continuous flow in open microfluidics using controlled evaporation.* Lab on a Chip, 2005. **5**(12): p. 1355-1359.
15. Meister, A., et al., *Nanodispenser for attoliter volume deposition using atomic force microscopy probes modified by focused-ion-beam milling.* Applied Physics Letters, 2004. **85**(25): p. 6260-6262.
16. Maxwell, J.C., Collected Scientific Papers, 1890. **Vol. 11**.
17. Langstroth, G.O., C.H.H. Diehl, and E.J. Winhold, *The Evaporation of Droplets in Still Air.* Canadian Journal of Research Section a-Physical Sciences, 1950. **28**(6): p. 580-595.
18. Poulard, C., G. Guena, and A.M. Cazabat, *Diffusion-driven evaporation of sessile drops.* Journal of Physics-Condensed Matter, 2005. **17**(49): p. S4213-S4227.
19. Picknett, R.G. and R. Bexon, *Evaporation of Sessile or Pendant Drops in Still Air.* Journal of Colloid and Interface Science, 1977. **61**(2): p. 336-350.
20. Birdi, K.S. and D.T. Vu, *Wettability and the Evaporation Rates of Fluids from Solid-Surfaces.* Journal of Adhesion Science and Technology, 1993. **7**(6): p. 485-493.
21. Birdi, K.S., D.T. Vu, and A. Winter, *A Study of the Evaporation Rates of Small Water Drops Placed on a Solid-Surface.* Journal of Physical Chemistry, 1989. **93**(9): p. 3702-3703.
22. Bourges, C. and M.E.R. Shanahan, *Influence of Evaporation on the Contact-Angle of Water Drops.* Comptes Rendus De L Academie Des Sciences Serie Ii, 1993. **316**(3): p. 311-316.
23. Bourgesmonnier, C. and M.E.R. Shanahan, *Influence of Evaporation on Contact-Angle.* Langmuir, 1995. **11**(7): p. 2820-2829.
24. Cordeiro, R.M. and T. Pakula, *Behavior of evaporating droplets at nonsoluble and soluble surfaces: Modeling with molecular resolution.* Journal of Physical Chemistry B, 2005. **109**(9): p. 4152-4161.
25. Erbil, H.Y., G. McHale, and M.I. Newton, *Drop evaporation on solid surfaces: Constant contact angle mode.* Langmuir, 2002. **18**(7): p. 2636-2641.
26. Fang, X.H., et al., *Factors controlling the drop evaporation constant.* Journal of Physical Chemistry B, 2005. **109**(43): p. 20554-20557.
27. McHale, G., et al., *Evaporation and the wetting of a low-energy solid surface.* Journal of Physical Chemistry B, 1998. **102**(11): p. 1964-1967.
28. Rowan, S.M., M.I. Newton, and G. McHale, *Evaporation of Microdroplets and the Wetting of Solid-Surfaces.* Journal of Physical Chemistry, 1995. **99**(35): p. 13268-13271.

29. Shanahan, M.E.R., *Is a sessile drop in an atmosphere saturated with its vapor really at equilibrium?* Langmuir, 2002. **18**(21): p. 7763-7765.
30. McHale, G., et al., *Analysis of shape distortions in sessile drops.* Langmuir, 2001. **17**(22): p. 6995-6998.
31. Pham, N.T., et al., *Application of the quartz crystal microbalance to the evaporation of colloidal suspension droplets.* Langmuir, 2004. **20**(3): p. 841-847.
32. McKenna, L., et al., *Compressional acoustic wave generation in microdroplets of water in contact with quartz crystal resonators.* Journal of Applied Physics, 2001. **89**(1): p. 676-680.
33. Arcamone, J., et al, *Evaporation of Femtoliter Sessile Droplets Monitored with Nanomechanical Mass Sensors.* Journal of Physical Chemistry B, 2007. **111**(45): p. 13020-13027.
34. Bonaccurso, E. and H.J. Butt, *Microdrops on atomic force microscope cantilevers: Evaporation of water and spring constant calibration.* Journal of Physical Chemistry B, 2005. **109**(1): p. 253-263.
35. Haschke, T., et al., *Sessile-drop-induced bending of atomic force microscope cantilevers: a model system for monitoring microdrop evaporation.* Journal of Micromechanics and Microengineering, 2006. **16**(11): p. 2273-2280.
36. Kern, R. and P. Muller, *Deformation of an Elastic Thin Solid Induced by a Liquid Droplet.* Surface Science, 1992. **264**(3): p. 467-494.
37. Spaepen, F., *Substrate curvature resulting from the capillary forces of a liquid drop.* Journal of the Mechanics and Physics of Solids, 1996. **44**(5): p. 675-681.
38. White, L.R., *The contact angle on an elastic substrate. 1. The role of disjoining pressure in the surface mechanics.* Journal of Colloid and Interface Science, 2003. **258**(1): p. 82-96.
39. Huang, J., et al., *Capillary wrinkling of floating thin polymer films.* Science, 2007. **317**(5838): p. 650-653.
40. Cleveland, J.P., et al., *A Nondestructive Method for Determining the Spring Constant of Cantilevers for Scanning Force Microscopy.* Review of Scientific Instruments, 1993. **64**(2): p. 403-405.
41. Golovko, D.S., et al., *Nondestructive and noncontact method for determining the spring constant of rectangular cantilevers.* Review of Scientific Instruments, 2007. **78**(4).
42. Rusanov, A.I., A.K. Shchekin, and D.V. Tatyanenko, *The line tension and the generalized Young equation: the choice of dividing surface.* Colloids and Surfaces a-Physicochemical and Engineering Aspects, 2004. **250**(1-3): p. 263-268.

43. Collins, R.E. and C.E. Cooke, *Fundamental Basis for the Contact Angle and Capillary Pressure.* Transactions of the Faraday Society, 1959. **55**(9): p. 1602-1606.
44. Everett, D.H., *Some Thermodynamic Aspects of Wetting and Adhesion.* Pure and Applied Chemistry, 1980. **52**(5): p. 1279-1293.
45. Li, T., *Hydrostatics in Various Gravitational Fields.* Journal of Chemical Physics, 1962. **36**(9): p. 2369-&.
46. Butt, H.J., D.S. Golovko, and E. Bonaccurso, *On the derivation of Young's equation for sessile drops: Nonequilibrium effects due to evaporation.* Journal of Physical Chemistry B, 2007. **111**(19): p. 5277-5283.
47. Young, T., Philos. Trans. R. Soc. London, 1805. **95**: p. 65.
48. McNutt, J.E. and G.M. Andes, *Relationship of the Contact Angle to Interfacial Energies.* Journal of Chemical Physics, 1959. **30**(5): p. 1300-1303.
49. Jameson, G.J. and M.C.G. Delcerro, *Theory for Equilibrium Contact-Angle between a Gas, a Liquid and a Solid.* Journal of the Chemical Society-Faraday Transactions I, 1976. **72**: p. 883-895.
50. Poulard, C., O. Benichou, and A.M. Cazabat, *Freely receding evaporating droplets.* Langmuir, 2003. **19**(21): p. 8828-8834.
51. Schwartz, A.M. and S.B. Tejada, *Studies of Dynamic Contact Angles on Solids.* Journal of Colloid and Interface Science, 1972. **38**(2): p. 359-&.
52. Rowan, S.M., et al., *Evaporation of microdroplets of three alcohols.* Journal of Physical Chemistry B, 1997. **101**(8): p. 1265-1267.
53. Kim, J.H., S.I. Ahn, and W.C. Zin, *Evaporation of water droplets on polymer surfaces.* Langmuir, 2007. **23**(11): p. 6163-6169.
54. Erbil, H.Y. and R.A. Meric, *Evaporation of sessile drops on polymer surfaces: Ellipsoidal cap geometry.* Journal of Physical Chemistry B, 1997. **101**(35): p. 6867-6873.
55. Soolaman, D.M. and H.Z. Yu, *Water microdroplets on molecularly tailored surfaces: Correlation between wetting hysteresis and evaporation mode switching.* Journal of Physical Chemistry B, 2005. **109**(38): p. 17967-17973.
56. Ruiz, O.E. and W.Z. Black, *Evaporation of water droplets placed on a heated horizontal surface.* Journal of Heat Transfer-Transactions of the Asme, 2002. **124**(5): p. 854-863.
57. Degennes, P.G., *Wetting - Statics and Dynamics.* Reviews of Modern Physics, 1985. **57**(3): p. 827-863.
58. Cachile, M., O. Benichou, and A.M. Cazabat, *Evaporating droplets of completely wetting liquids.* Langmuir, 2002. **18**(21): p. 7985-7990.

59. Langmuir, I., *The evaporation of small spheres.* Physical Review, 1918. **12**(5): p. 368-370.
60. Erbil, H.Y. and M. Dogan, *Determination of diffusion coefficient-vapor pressure product of some liquids from hanging drop evaporation.* Langmuir, 2000. **16**(24): p. 9267-9273.
61. Grandas, L., et al., *Experimental study of the evaporation of a sessile drop on a heat wall. Wetting influence.* International Journal of Thermal Sciences, 2005. **44**(2): p. 137-146.
62. David, S., K. Sefiane, and L. Tadrist, *Experimental investigation of the effect of thermal properties of the substrate in the wetting and evaporation of sessile drops.* Colloids and Surfaces a-Physicochemical and Engineering Aspects, 2007. **298**(1-2): p. 108-114.
63. Hu, H. and R.G. Larson, *Analysis of the effects of Marangoni stresses on the microflow in an evaporating sessile droplet.* Langmuir, 2005. **21**(9): p. 3972-3980.
64. Hu, H. and R.G. Larson, *Analysis of the microfluid flow in an evaporating sessile droplet.* Langmuir, 2005. **21**(9): p. 3963-3971.
65. Kavehpour, P., B. Ovryn, and G.H. McKinley, *Evaporatively-driven Marangoni instabilities of volatile liquid films spreading on thermally conductive substrates.* Colloids and Surfaces a-Physicochemical and Engineering Aspects, 2002. **206**(1-3): p. 409-423.
66. Berger, R., et al., *Micromechanical thermogravimetry.* Chemical Physics Letters, 1998. **294**(4-5): p. 363-369.
67. Berger, R., et al., *Micromechanics: A toolbox for femtoscale science: "Towards a laboratory on a tip".* Microelectronic Engineering, 1997. **35**(1-4): p. 373-379.
68. Berger, R., et al., *Thermal analysis using a micromechanical calorimeter.* Applied Physics Letters, 1996. **69**(1): p. 40-42.
69. von Bahr, M., F. Tiberg, and B. Zhmud, *Oscillations of sessile drops of surfactant solutions on solid substrates with differing Hydrophobicity.* Langmuir, 2003. **19**(24): p. 10109-10115.
70. Yarin, A.L., *Drop impact dynamics: Splashing, spreading, receding, bouncing.* Annual Review of Fluid Mechanics, 2006. **38**: p. 159-192.
71. Rioboo, R., M. Marengo, and C. Tropea, *Time evolution of liquid drop impact onto solid, dry surfaces.* Experiments in Fluids, 2002. **33**(1): p. 112-124.
72. Rein, M., *Phenomena of Liquid-Drop Impact on Solid and Liquid Surfaces.* Fluid Dynamics Research, 1993. **12**(2): p. 61-93.
73. Sarid, D., *Exploring Scanning Probe Microscopy with Mathematica*. 1997, New York: Oxford University Press.
74. Butt, H.J. and M. Jaschke, *Calculation of Thermal Noise in Atomic-Force Microscopy.* Nanotechnology, 1995. **6**(1): p. 1-7.

75. Butt, H.J., et al., *Scan Speed Limit in Atomic Force Microscopy.* Journal of Microscopy-Oxford, 1993. **169**: p. 75-84.
76. Stoney, G.G., *The tension of metallic films deposited by electrolysis.* Proceedings of the Royal Society of London Series a-Containing Papers of a Mathematical and Physical Character, 1909. **82**(553): p. 172-175.
77. Cappella, B. and G. Dietler, *Force-distance curves by atomic force microscopy.* Surface Science Reports, 1999. **34**(1-3): p. 1-+.
78. Gould, S.A.C., et al., *The Atomic Force Microscope - a Tool for Science and Industry.* Ultramicroscopy, 1990. **33**(2): p. 93-98.
79. Preuss, M. and H.J. Butt, *Direct measurement of particle-bubble interactions in aqueous electrolyte: Dependence on surfactant.* Langmuir, 1998. **14**(12): p. 3164-3174.
80. Gillies, G., et al., *Contact angles and wetting behaviour of single micron-sized particles.* Journal of Physics-Condensed Matter, 2005. **17**(9): p. S445-S464.
81. Ulmke, H., T. Wriedt, and K. Bauckhage, *Piezoelectric droplet generator for the calibration of particle-sizing instruments.* Chemical Engineering & Technology, 2001. **24**(3): p. 265-268.
82. Weber, A., R. Pockelmann, and C.P. Klages, *Electrical and optical properties of amorphous fluorocarbon films prepared by plasma polymerization of perfluoro-1,3-dimethylcyclohexane.* Journal of Vacuum Science & Technology a-Vacuum Surfaces and Films, 1998. **16**(4): p. 2120-2124.
83. Burnham, N.A., et al., *Comparison of calibration methods for atomic-force microscopy cantilevers.* Nanotechnology, 2003. **14**(1): p. 1-6.
84. Butt, H.J., B. Cappella, and M. Kappl, *Force measurements with the atomic force microscope: Technique, interpretation and applications.* Surface Science Reports, 2005. **59**(1-6): p. 1-152.
85. Ralston, J., et al., *Atomic force microscopy and direct surface force measurements - (IUPAC technical report).* Pure and Applied Chemistry, 2005. **77**(12): p. 2149-2170.
86. Sader, J.E., *Parallel Beam Approximation for V-Shaped Atomic-Force Microscope Cantilevers.* Review of Scientific Instruments, 1995. **66**(9): p. 4583-4587.
87. Sader, J.E., *Frequency response of cantilever beams immersed in viscous fluids with applications to the atomic force microscope.* Journal of Applied Physics, 1998. **84**(1): p. 64-76.
88. Sader, J.E., J.W.M. Chon, and P. Mulvaney, *Calibration of rectangular atomic force microscope cantilevers.* Review of Scientific Instruments, 1999. **70**(10): p. 3967-3969.

89. Green, C.P., et al., *Normal and torsional spring constants of atomic force microscope cantilevers.* Review of Scientific Instruments, 2004. **75**(6): p. 1988-1996.
90. Higgins, M.J., et al., *Noninvasive determination of optical lever sensitivity in atomic force microscopy.* Review of Scientific Instruments, 2006. **77**(1).
91. Hutter, J.L. and J. Bechhoefer, *Calibration of Atomic-Force Microscope Tips.* Review of Scientific Instruments, 1993. **64**(7): p. 1868-1873.
92. Senden, T.J. and W.A. Ducker, *Experimental-Determination of Spring Constants in Atomic-Force Microscopy.* Langmuir, 1994. **10**(4): p. 1003-1004.
93. Craig, V.S.J. and C. Neto, *In situ calibration of colloid probe cantilevers in force microscopy: Hydrodynamic drag on a sphere approaching a wall.* Langmuir, 2001. **17**(19): p. 6018-6022.
94. Notley, S.M., S. Biggs, and V.S.J. Craig, *Calibration of colloid probe cantilevers using the dynamic viscous response of a confined liquid.* Review of Scientific Instruments, 2003. **74**(9): p. 4026-4032.
95. Maeda, N. and T.J. Senden, *A method for the calibration of force microscopy cantilevers via hydrodynamic drag.* Langmuir, 2000. **16**(24): p. 9282-9286.
96. Torii, A., et al., *A method for determining the spring constant of cantilevers for atomic force microscopy.* Measurement Science & Technology, 1996. **7**(2): p. 179-184.
97. Bonaccurso, E., F. Schonfeld, and H.J. Butt, *Electrostatic forces acting on tip and cantilever in atomic force microscopy.* Physical Review B, 2006. **74**(8).
98. Bonaccurso, E. and G. Gillies, *Revealing contamination on AFM cantilevers by microdrops and microbubbles.* Langmuir, 2004. **20**(26): p. 11824-11827.
99. www.comsol.com.
100. Lam, C.N.C., et al., *Study of the advancing and receding contact angles: liquid sorption as a cause of contact angle hysteresis.* Advances in Colloid and Interface Science, 2002. **96**(1-3): p. 169-191.
101. Good, R.J., *Contact-Angle, Wetting, and Adhesion - a Critical-Review.* Journal of Adhesion Science and Technology, 1992. **6**(12): p. 1269-1302.

List of Abbreviations

AFM	atomic force microscope
CCA	constant contact angle
CCR	constant contact radius
FEM	finite element method
NI	negative inclination
PEDG	piezo electric drop generator
PEEK	polyetheretherketon
PPFC	perfluoro-1,3-dimethylcyclohexane
PSD	position sensitive device
QCM	quartz crystal microbalance
RH	relative humidity
R-PIA	reversed particle interaction apparatus
SS	stick-slip

Acknowledgements

This thesis would not have appeared without numerous help and constant support of the following people.

Prof. Hans-Jürgen Butt is gratefully acknowledged for providing me with priceless opportunity to work and to explore in the broad scientific field of his group. Fruitful discussions with him and his tolerance while answering my numerous questions deepened significantly my understanding of the surface science problems.

I would like to express a special invaluable gratitude to my supervisor Dr. Elmar Bonaccurso. His constant patience and attention, broad erudition, versatility and tactful approach in scientific work and everyday life inspired me and made me successively rethink of many of my views in both science and life.

I want to say a big "thank you" to Andreas Best who helped me a lot in the developing and construction of my experimental setup. Dr. Karsten Büscher is deeply thanked for his initial help during my first steps towards device designing procedures.

Many thanks go to Dr. Michael Kappl for teaching me how to make a device measure what I want. Again, my first steps in LabView programming would not be possible without his constant support. Norbert Höhn is deeply acknowledged for helping me to actually see what happens in front of my CCD camera during experiments.

I want to express a separated gratitude to Prof. Roberto Raiteri and Paolo Bonanno with Simone Lorenzoni who helped me throughout my Italian scientific, and not only, journey providing me with a lot of assistance and farsight. I deeply appreciated the kind working atmosphere there and sympathetic people in Genoa and in the university of Genoa, especially in the evening. Dr. Rüdiger Berger is deeply thanked for supporting my trip to Genoa and numerous discussions during my PhD time.

Thomas Haschke and Prof. Wolfgang Wiechert are thanked for "numerical" spring constant calibration of cantilevers and fruitful collaboration.

Finally, I would like to thank to all the AK Butt group members for their friendly atmosphere, constant support and tenderness, coffee corner free time and talks, soccer fun and the all time spent together in general. Thank you!

For financial support during my PhD time the German Research Society and the Max Planck Society are gratefully acknowledged. Vigoni Programme is thanked for supporting my trip to Genoa.